

# Direct inversion of earthquake first motions for both the stress tensor and focal mechanisms and application to southern California

Geoffrey A. Abers

Department of Earth Sciences, Boston University, Boston Massachusetts, USA

John W. Gephart

Institute for the Study of Continents, Cornell University, Ithaca New York, USA

**Abstract.** In inverting populations of focal mechanisms to estimate stress, misfits may arise owing to (1) errors in determining the fault plane solutions and (2) real variations in the state of stress. Among a number of techniques that invert for stress, most effectively regard only the latter and only indirectly describe the former through statistical means so make it difficult to differentiate real stress variations from noisy data. Ambiguity arises because realistic methods for determining focal mechanisms for small earthquakes depend on *P* wave first motions in a highly nonlinear manner, which is difficult to propagate into stress inversions. To address these issues, we present a new method for constraining stress tensors, in which first-motion observations are directly inverted for stress without assuming that focal mechanisms are known. The technique produces estimates of four stress parameters, a suite of focal mechanisms consistent with both the stress tensor and the first motions, and estimates of the uncertainty in stress. It also provides a natural test of the stress homogeneity hypothesis and a means to identify those earthquakes whose first motions are not consistent with a homogeneous stress tensor. When tested against artificial data, the method correctly recovers input stresses and yields uncertainties that depend upon both data distribution and reliability of first motion picks, as expected. Utilizing first motions from the southern California catalog, the method is applied to several clusters and aftershock sets, from 1981 to 1992. Typical uncertainties in stress orientation exceed 20–30° at the 95% confidence level, resulting from ~5% mispick rates typical of even the cleanest data. These uncertainties exceed some previous estimates for similar populations, presumably because they account for focal mechanism uncertainties, and perhaps indicating that some previously reported stress variations are not statistically significant. Most populations are found to be internally consistent with a homogeneous stress field, the most significant exceptions being aftershock sequences of some major earthquakes. In at least one case, the 1992 Landers sequence, aftershocks at the north end of the rupture zone appear to reflect exceedingly heterogeneous stresses. Overall, the method provides a useful and robust approach for evaluating stress constraints provided by *P* wave first motions.

## 1. Introduction

Earthquakes occur in response to deviatoric stress [Reid, 1910]. Despite nearly a century of research, the state of stress of the Earth and its relation to earthquakes are poorly known. Some workers have presumed that the brittle crust is relatively strong [e.g., Brace and Kohlstedt, 1980], and the faults that slip are ones that are optimally oriented relative to the ambient stress field [Anderson, 1951]. However, several recent studies have suggested that the relationship is more complex between the slip along major faults and the stresses that cause it, notably that weak faults may slip in nonoptimum orientations of relatively low shear stress [e.g., Zoback *et al.*, 1987; Rice,

1992]. In these cases, preexisting weaknesses can lead to nonoptimal fault geometries and diverse focal mechanisms even in homogeneous stress fields. Thus variation in orientations among a population of focal mechanisms may occur owing to at least three possible causes: (1) local variations in stress fields, (2) the presence of preexisting faults of varying strength that slip in response to the same stress field, or (3) errors in the determination of fault plane orientations.

A number of inverse techniques have been devised in recent years to constrain the stress tensor from earthquake focal mechanisms. These implicitly regard earthquakes as passive markers of stress and attempt to estimate the best uniform stress field from multiple events within limited space-time windows. The basic constraint is that the inferred direction of slip reflects the orientation of shear stress on each fault plane, neglecting relatively small local heterogeneities that are treated as noise (including possible minor effects of nonlinearity and anisotropy postulated by some [Twiss and Unruh, 1998]). The

Copyright 2001 by the American Geophysical Union.

Paper number 2001JB000437.  
0148-0227/01/2001JB000437\$09.00

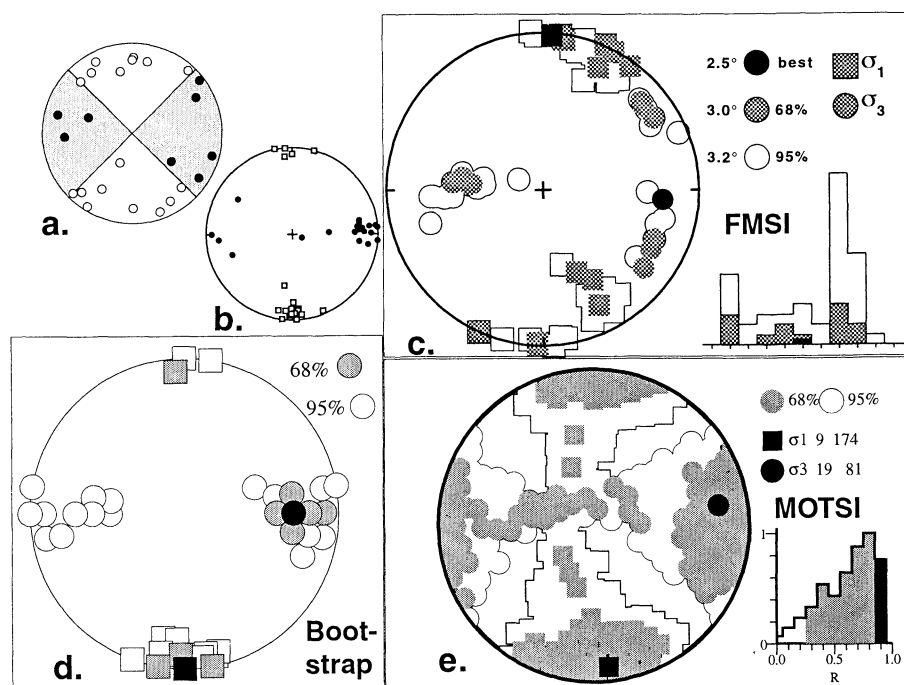


**Figure 1.** Artificial example designed to highlight biases in confidence limits when first-motion uncertainties are not considered. (a) Fiducial focal mechanism sampled by the illustrated ray geometry. Compressional quadrants are shaded. First motions are then perturbed randomly 50 times via a statistical model resembling Figure A1 ( $\gamma = 0.05$ ,  $\alpha = 0.1$ ), and fault plane solutions are redetermined. (b) Fifty  $P$  and  $T$  axes, open and solid circles, for the perturbed fault plane solutions. Their variation reflects only noise due to errors in first motions. (c) Inversion of the focal mechanisms in Figure 1b using FMSI [Gephart, 1990b]. (d) Inversion of focal mechanisms in Figure 1b using the grid search method of Michael [1987a] with bootstrap confidence estimates. (e) Inversion of first motions from Figure 1b using MOTSI. In each case, confidence regions for  $\sigma_1$  and  $\sigma_3$  are shown by squares and circles, respectively, with 68% and 95% confidence limits highlighted. Figures 1c and 1d show unrealistically small confidence limits. These data only consist of a single focal mechanism (plus noise) and so should be unable to constrain the  $\sigma_1$  and  $\sigma_3$  axes each to better than their respective quadrants [McKenzie, 1969].

inversions constrain a dimensionless deviatoric stress tensor, characterized by four independent parameters, three defining the orientations of principal stress axes ( $\sigma_1 \geq \sigma_2 \geq \sigma_3$ ) and a fourth which fixes the magnitude of  $\sigma_2$  relative to  $\sigma_1$  and  $\sigma_3$ ,

$$R = (\sigma_2 - \sigma_1) / (\sigma_3 - \sigma_1). \quad (1)$$

By combining the information among several earthquake focal mechanisms, which indicate the direction of slip on either of two possible fault planes (and are assumed to record directions of shear stress within a uniform stress field), one can invert for these four stress parameters. Gephart and Forsyth [1984] and Gephart [1990a, 1990b] present such an inverse procedure, following principles recognized much earlier by Wallace [1951], Bott [1959], and McKenzie [1969]. Several other workers have derived independent procedures for inferring stresses from fault orientation data [e.g., Angelier, 1984; Michael, 1984].

One of the difficulties of these stress inversion techniques is that the analysis is based on input data with complex uncertainties, earthquake focal mechanisms. While it is possible to realistically assess the uncertainty of the stress inversion procedure on the basis of known focal mechanisms, there is rarely a full accounting of the real uncertainty in the determination of the focal mechanisms themselves. For most small events, focal mechanisms are determined from  $P$  wave first motions by

fitting orthogonal nodal planes [e.g., Reasenber and Oppenheimer, 1985], a highly nonlinear process subject to a variety of errors [e.g., Aki, 1976; Dillinger *et al.*, 1972]. Irregular sampling of the focal sphere can lead to complicated sets of feasible solutions that are not easily describable. Compounding such uncertainties, the ray takeoff angles used to compare  $P$  waves with nodal planes depend on an imperfectly known seismic velocity structure, leading to additional error. Because of the complicated nature of these uncertainty distributions, it is difficult to incorporate them into the stress inversions in any direct way.

Some diversity of focal mechanisms is required to adequately constrain stresses [e.g., Gephart, 1998], but often it is difficult to distinguish real diversity of fault plane orientations from scatter caused by noisy data. This problem is illustrated in Figure 1. Here we generate an artificial data set which should place very little constraint on the stress tensor because all "true" mechanisms are identical: in this situation, only the quadrants containing the maximum and minimum principal stresses can be known [McKenzie, 1969]. Such a situation may arise where a single fault produces all earthquakes. Still, with the addition of reasonable noise among the first motions, conventional stress inversions [Gephart and Forsyth, 1984; Michael, 1987a] produce somewhat well-constrained estimates of stress with unrealistically small uncertainties. The apparent diversity among focal mechanisms owing to the contribution

of noise in the first motion picks is not directly considered in either of the two inversions tested here except through statistical inference, leading to these underestimates of uncertainty. Thus, while a certain amount of diversity among focal mechanisms is needed in order to limit the range of acceptable stresses, if the inferred diversity is not real then the use of those data can be misleading. It is difficult to distinguish the situation in Figure 1 from actual variations in focal mechanisms. Although the case shown in Figure 1 is chosen for its pathological nature, with no real diversity of focal mechanisms, it illustrates a potential limitation of conventional inverse techniques.

For these reasons, we explore here the possibility of resolving the four-parameter stress tensor directly from first motions, thus circumventing the reliance on the intermediate step of independently compiling focal mechanisms. Previously, *Rivera and Cisternas* [1990] proposed a linearized scheme to solve this problem; however, given the highly nonlinear nature of the problem, the formal errors determined from linearized approximations may not realistically reflect the actual uncertainties. *Horiuchi et al.* [1995] developed a nonlinear scheme similar to ours, but their approach did not include a method for error assessment. Our approach [Abers and Gephart, 1995, 1997; Gephart and Abers, 1996] yields estimates of stress tensor elements with more complete uncertainties, in that they incorporate those associated with determining focal mechanisms. As by-products, it also provides estimates of focal mechanisms and a measure of the degree of degradation in fit imposed by enforcing a uniform stress field over the whole population. Our method is a first motion stress inversion (termed MOTSI), but the approach is easily generalized to other sorts of observations (*S* wave polarities, waveform amplitudes, etc.) and could be extended in the future.

## 2. Method

### 2.1. Estimating Stress From First Motions

**2.1.1. Overview.** Our MOTSI inverse scheme follows the focal mechanism stress inversion (FMSI) algorithm of *Gephart* [1990b] in exploring a four-parameter stress space on a grid in search of a best fitting stress model and confidence estimates. In MOTSI we compute two nested grid searches in order to identify the best stresses and focal mechanisms (Figure 2). The first, outer search is conducted over a wide range of the four stress parameters, three stress directions and *R*, sequentially testing independent stress models (Figure 2a). The sec-

ond, inner search, is conducted once for each stress model over a grid of fault planes (Figure 2b), and identifies for each event the focal mechanisms that best fit the first motions (Figure 2c). Thus we continuously test stress-consistent focal mechanisms against first motions. By starting with raw first-motion data we hope to avoid the prospect that incorrectly assigned focal mechanisms (from limited or conflicting first motions) might bias the results in favor of heterogeneous stresses. This allows us to better assess the requirement of

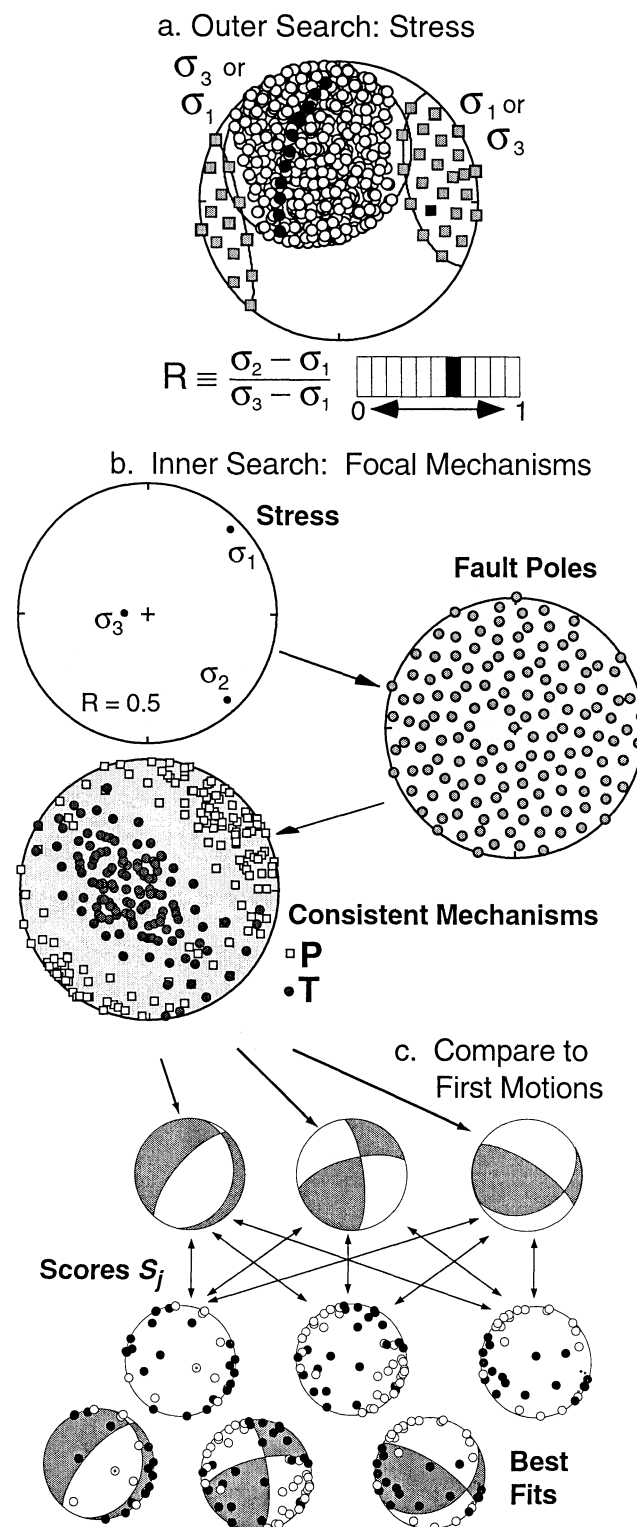


**Figure 2.** Illustration of the MOTSI procedure, discussed in the text. (a) An outer loop that explores all stresses in a grid of primary stresses (squares), orthogonal secondary stresses (circles), and *R* values. Four parameters define each stress tensor. (b) For each stress tensor, an inner loop generating a suite of stress-consistent focal mechanisms (denoted by *P*, *T* axes) from a uniform grid of fault poles. For each fault pole (two parameters), a given stress tensor predicts a unique slip vector and hence unique focal mechanism. (c) Comparison of each stress-consistent focal mechanism to each earthquake's first motions and assignment of score  $S_j$  (equation (6)). The mechanism corresponding to the highest  $S_j$  for each event is selected for the event, and the resultant  $S_j$  are appropriately summed to provide an aggregate score (equation (7)) for that stress tensor. This process is repeated to determine scores for all possible stresses.

homogeneity, owing to an improved treatment of the real uncertainty of the data. It also provides a suite of focal mechanisms that is simultaneously consistent with a single stress tensor and fits the first motions as closely as possible.

**2.1.2. Search scheme.** We adopt a grid search approach that systematically varies the principal stress directions and  $R$  over the full range of model space [Gephart, 1990b]. Specifically, the algorithm tests orientations of a "primary" principal stress axis over a uniform spherical grid of directions, utilizing the uniform spherical mesh of Baumgardner and Frederickson [1985]. The primary principal stress may be either  $\sigma_1$  or  $\sigma_3$ ; the other is the secondary principal stress. For each such primary stress orientation (defined by angles  $\Theta$ ,  $\Psi$  [Gephart, 1990b]), it tests secondary stress axes at even increments of angle ( $\Phi$ ) in the orthogonal plane, and search over even increments of  $R$ . Each unique combination, or node, of four parameters represents a stress model to be tested. In most examples given below, a trial grid has density of  $8\text{-}10^\circ$  node spacing in both primary and secondary stresses, and  $R$  varies from 0 to 1 at increments of 0.1, resulting in a total of 64,521 stress models being tested (discounting redundant stresses at  $R=0$  or  $R=1$ ). Such spacing is generally much smaller than the resulting stress uncertainties, so a denser grid is not warranted.

At each stress model (i.e., at each node of the outer search) we estimate the fit of first-motion observations by testing a range of focal mechanisms. The suite of focal mechanisms searched is by definition consistent with the stress model at hand; among these focal mechanisms, we find the one that is most in agreement with first motions for each event. The measure of fitness between first motions and mechanisms is a weighted measure of the number of correctly picked first motions (see section 2.2). This is akin to the procedure of the program FPFIT [Reasenberg and Oppenheimer, 1985], which evaluates focal mechanisms from  $P$  wave first motions. However, the search includes only those focal mechanisms that are consistent with the current stress tensor: the fault plane can have any arbitrary orientation, but the slip vector must be aligned with the shear stress direction predicted by the stress model (applying equation (7) of Gephart [1990a]). A suite of fault plane poles evenly samples all possible orientations, utilizing the spherical mesh algorithms of Baumgardner and Frederickson [1985], resulting in a grid of 321 fault poles at  $8\text{-}10^\circ$  spacing (Figure 2b). The best possible fit to the entire suite of events is then evaluated for each stress model by combining fitness estimates from individual events. On a Sparc-Ultra 10 workstation, a complete grid search in stress and focal mechanism took roughly 45 min per 1000 first motions, with 96% of CPU time in a subroutine that evaluates misfit to first motions.

A separate routine, MOTSI-FP, finds best fitting focal mechanisms in the same way but without imposing the stress constraint, essentially as in FPFIT [Reasenberg and Oppenheimer, 1985] but using the same description of misfit as in the present study. This allows us to directly assess the effects of the stress constraint on suites of focal mechanisms and allows a formal test of the hypothesis of uniform stress within populations.

## 2.2. Evaluation of Fit to First Motions

First motions are discrete measurements of the sign of radiated amplitude at a finite number of points on the focal sphere, and highly irregular suites of focal mechanisms can satisfy these data to a similar degree. Even for favorable ray distributions, the first motions themselves can be systematically mis-

identified, especially when background noise is high [Aki, 1976]. Also, the associated takeoff angles can exhibit systematic biases, especially when downgoing rays are used at regional distances. These problems have led to a variety of amplitude-dependent schemes for characterizing the probability distribution of first motion data [e.g., Knopoff, 1960; Pope, 1972; Brillinger *et al.*, 1980]. In part, for these reasons, popular automated methods for determining focal mechanisms [e.g., Reasenberg and Oppenheimer, 1985; Guinn and Long, 1977] perform nonlinear grid searches and characterize the results as irregular confidence limits (e.g., populations of acceptable  $P$  and  $T$  axes).

The approach here follows those of Brillinger *et al.* [1980] and Pope [1972] and assumes that each first-motion observation is an independent datum and has a probability of being correct that can be numerically characterized a priori.

**2.2.1. Individual event.** Suppose event  $j$  has  $N_j$  first-motion measurements ( $j = 1, \dots, M$ ;  $M$  is the number of events), of which  $L_j$  ( $\leq N_j$ ) are consistent with a given focal mechanism solution. Let  $d_{ij}$  be a random variable that describes the first motion for the  $i$ th observation of the  $j$ th event ( $i = 1, \dots, N_j$ ). Specifically,  $d_{ij} = 1$  if the pick is correct, or  $d_{ij} = 0$  otherwise, so that

$$L_j = \sum_{i=1}^{N_j} d_{ij}. \quad (2)$$

The  $d_{ij}$  are Bernoulli trials, observations that have probability  $p_{ij}$  of being 1 (correct pick) and  $1-p_{ij}$  of being 0 (incorrect pick). For useful data,  $p_{ij}$  are close to 1, and for completely uninformative observations,  $p_{ij} = 0.5$  and in general, are different for each datum (see Appendix A). The  $d_{ij}$  have a Binomial distribution for which  $\text{Var}\{d_{ij}\} = p_{ij}(1-p_{ij})$  is the variance of a single pick [e.g., Larson and Marx, 1981]. Then

$$\text{Var}\{L_j\} = \sigma_j^2 = \sum_{i=1}^{N_j} p_{ij}(1-p_{ij}). \quad (3)$$

$L_j$ , a sum of binomial-distributed data, should become approximately normally distributed for large  $N_j$  with variance  $\sigma_j^2$  by the DeMoivre-Laplace limit theorem. Hence for each event we define the fit of a focal mechanism to first motions with the statistic

$$S_j = L_j / \sigma_j, \quad (4)$$

which should have unit variance. Brillinger *et al.* [1980] developed a similar statistic via maximum likelihood analysis (their equation (13)). For individual events the value of  $S_j$  will be largest for the best fitting focal mechanism and will be lower for others.

To verify the form of the probability distribution, Figure 3 shows histograms of  $L_j/N_j$  for two samples of southern California data of differing quality. If all data have the same distribution, then  $L_j/N_j$  should have a binomial distribution and their mean should be an unbiased estimate of uncertainty in each individual datum. These histograms approximate a binomial distribution, supporting the inference of binomial statistics. Still, chi-square tests indicate that a simple binomial distribution differs significantly (at 95% confidence) from these data, likely because the  $p_{ij}$  vary from pick to pick. This misfit motivates a somewhat more complex model for  $p_{ij}$  that

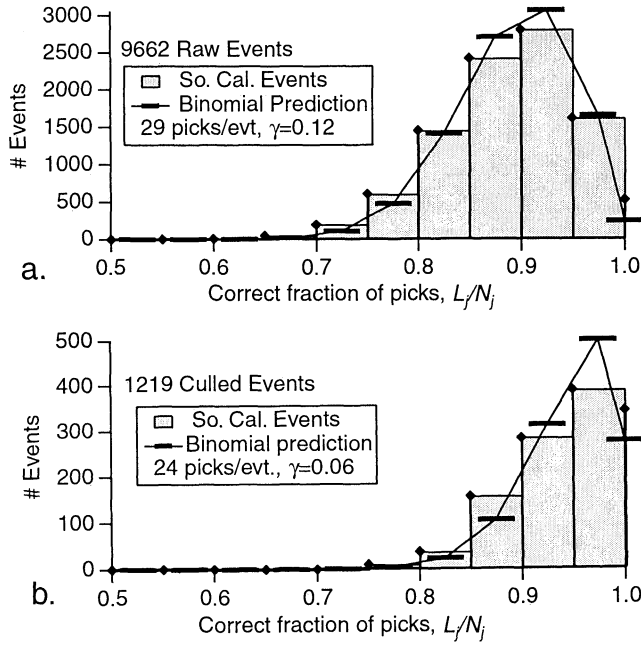


**Figure 3.** Fraction of picks consistent with focal mechanisms, per event, compared to predictions of simple binomial probability distributions. (a) All observed 9662 focal mechanisms in the southern California clusters studied. (b) The 1219 southern California events selected by culling procedures described in text. Events are compared to focal mechanisms determined without regard to stress using MOTSI-FP. Horizontal bars show a prediction of this success rate, assuming simple binomial distribution with the listed number of picks per event and a mispick rate for individual picks  $\gamma$ , matching the averages for each cluster. Note overall consistency of the simple binomial probability distribution, indicating overall appropriateness of the assumed error model. Remaining misfit likely reflects varying numbers of picks per event and variable data quality.

takes into account the lesser reliability of near-nodal arrivals, as discussed in Appendix A.

**2.2.2. Event suites.** The same approach evaluates fit of a stress model to first motions from several events. Given the best scores for a suite of events, we define a global misfit  $S$  as

$$S = \sum_j S_j \sigma_j / \sqrt{\sum_j \sigma_j^2}, \quad (5)$$

which again should be normally distributed with unit variance for large numbers of first motions. These calculations are made from the best fitting focal mechanism for each event among those that are consistent with a given stress field; thus  $S$  represents the largest possible score for a given stress model. As can be seen by comparing equations (2)-(5), this measure is simply the number of correctly predicted first motions normalized to its predicted standard deviation.

In summary, the inner loop process of determining the best focal mechanism for each event (Figure 2c) becomes one of choosing that mechanism that produces the largest  $S_j$ . The subsequent outer loop determines the best stress (Figure 2a) by selecting the stress tensor that produces the largest  $S$  from (5), given the suites of  $S_j$  and  $\sigma_j$ . Confidence limits are discussed below.

**2.2.3. Weighting.** In practice, the above procedure does not always select the best focal mechanism for each event when the distribution of first motions is poor. The problem is that, as defined above, near-nodal arrivals are nearly as important as those far from the node; an incorrect pick has a strong effect whether it is near a node or far from it. Because correct arrivals seem more likely far from nodes, we redefine  $S_j$  to a statistic that weights down low-probability (near nodal) arrivals:

$$S'_j = \frac{\sum_i w_{ij} d_{ij}}{\sqrt{\sum_i w_{ij}^2 p_{ij} (1 - p_{ij})}} = \frac{L'_j}{\sigma'_j} \quad (6)$$

with a global statistic for each stress tensor

$$S' = \sum_j S'_j \sigma'_j / \sqrt{\sum_j \sigma'^2_j} \quad (7)$$

for some set of weights  $w_{ij}$ . As before, this statistic has unit standard deviation and is normally distributed for large  $N = \sum_j N_j$ . The simple weighting scheme applied here sets

$$w_{ij} = 2p_{ij} - 1, \quad (8)$$

which assigns zero weight for nodal arrivals and positive weight elsewhere.

### 2.3. Estimates of Uncertainties

Conceptually, we imagine three sources of error: (1) the first motions may be incorrectly estimated, either in polarity or in ray location, (2) coverage of the focal sphere may be incomplete, leading to a wide range of incorrect focal mechanisms that nevertheless fit the first motions, and (3) an incomplete range in fault planes may lead to a wide range of stress tensors that fit the focal mechanism population. It may be argued that only error type 1 consists of true data noise, but all three should contribute to parameter uncertainties. A conventional nonlinear stress inversion method [Gephart, 1990b; Michael, 1987a] should be able to treat type 3 errors correctly by fully exploring the relation between stress parameter space and the fault planes actually observed. Such methods treat errors arising from error of types 1 and 2 by a statistical test of misfit to fault plane mechanism, either parametrically or inferred from bootstrap tests. Although these treatments may give the correct answers in many cases, it is not clear that they will always do so (e.g. Figure 1). By contrast, the MOTSI algorithm deals with error of type 2 in a manner similar to that of type 3, by directly exploring the complete parameter space with respect to focal mechanism. The errors in first motions are dealt with directly.

Confidence limits in stress are estimated in two steps. First, we determine the error rate present in each data subset. These estimates are made first by fitting focal mechanisms to the first motions (not considering stress, via MOTSI-FP) and then by examining the rate of first-motion misfit. This latter rate is estimated by dividing the number of correctly predicted polarities ( $L_j$ ) by the total number of picks ( $N_j$ ); the statistic  $L_j/N_j$  is an unbiased estimate of binomial probabilities [e.g., Larson and Marx, 1981] and commonly used in first-motion studies [e.g., Pope, 1972]. This procedure is repeated separately over each predicted radiation pattern amplitude range and fit to a

**Table 1.** Results From Stress Inversions<sup>a</sup>

Region	<i>M</i>	<i>N</i>	$\gamma$	<i>dS</i>	Confidence, % <sup>b</sup>	NFM	Acceptable Stresses <sup>c</sup>		$\sigma_1$		$\sigma_3$		<i>R</i>	ID
							68%	95%	Pl	Tr	Pl	Tr		
Banning deep	178	4657	0.0466	4.56	99.94	20	0.14	0.66	29	178	17	278	0.5	A
Banning shallow pre-1986	61	1611	0.0447	1.61	87.25	20	0.51	2.84	9	174	17	267	0.7	B
North Palm Springs	74	2093	0.0292	3.57	99.42	20	0.05	0.65	2	172	80	70	0.9	C
Banning shallow 1987-1991	118	3018	0.0440	3.15	98.70	20	0.17	1.47	7	166	62	270	0.7	D
Banning shallow 1993-1997	91	2375	0.0483	2.71	97.23	20	0.23	1.84	16	169	2	260	0.4	E
Cajon Pass	86	2359	0.0603	1.32	82.47	25	0.76	4.22	8	170	14	262	0.6	F
Pre Northridge	35	974	0.0914	0.88	73.31	20	2.47	9.99	3	188	66	91	0.7	G
San Andreas Fault	41	1130	0.0659	1.68	88.26	20	0.73	4.51	0	2	89	102	0.7	H
Santa Monica Bay	37	1216	0.0788	1.07	77.54	20	0.62	3.94	5	195	11	286	0.7	I
Upland aftershock	85	2206	0.0361	2.76	97.45	20	0.06	0.42	3	166	62	70	1.0	J
West LA Basin	57	1684	0.0920	1.73	88.94	20	1.55	7.34	6	28	53	291	0.6	K
Whittier aftershock	69	2096	0.0578	3.02	98.36	20	0.15	0.84	9	174	81	14	0.8	W
Coso pre-Ridgecrest	200	4733	0.0400	4.08	99.80	25	0.11	0.81	26	8	5	276	0.4	M
Elsinore Fault	62	1566	0.0524	1.92	91.27	20	1.82	7.10	6	1	3	270	0.5	N
Garlock Fault	47	1469	0.0504	1.77	89.46	20	0.18	2.13	66	186	1	278	0.2	P
San Jacinto Fault South	73	2130	0.0505	1.23	80.78	25	0.11	1.39	4	176	3	86	0.5	Q
White Wolf SW	43	1082	0.0595	2.40	95.52	20	0.41	3.38	17	356	56	112	0.8	R
White Wolf Central	102	3154	0.0364	1.97	91.82	25	0.48	2.29	4	176	3	86	0.7	S
White Wolf NE	36	1053	0.0364	1.54	86.19	25	0.61	2.94	30	352	12	89	0.2	T
Pre-Joshua Tree	51	1516	0.0462	1.19	80.00	25	0.56	3.56	13	195	3	286	0.2	L1
Joshua Tree Aftershocks	45	1399	0.0400	1.48	85.23	30	0.27	1.54	50	8	2	101	0	L2
Landers Aftershocks L2 area	109	3139	0.0747	1.90	91.04	25	0.39	1.44	40	28	0	298	0	L3
Landers South including L3	176	4903	0.0627	2.63	96.85	25	0.13	0.74	57	209	1	118	0	L4
Landers Central	78	2242	0.0651	2.88	97.91	25	0.20	0.96	24	203	1	113	0	L5
Landers North	99	2821	0.0499	11.27	100.00	25	0.04	0.17	41	96	1	5	0	L6
Landers Camp Rock	79	1963	0.0423	7.80	100.00	20	0.04	0.16	5	355	3	86	1.0	L6a
Landers Emerson	106	2761	0.0523	4.97	99.98	20	0.05	0.46	86	8	1	121	0.3	L6b

<sup>a</sup> *M*, number of events; *N*, number of first motions inverted, NFM, minimum number of first motions per event; Pl, plunge; Tr, trend. ID, designation of region on figures.

<sup>b</sup> Confidence level at which homogeneous stress assumption can be rejected, *dS* = 1.0 corresponds to 76% and *dS* = 2.0 corresponds to 92%.

<sup>c</sup> Percent of all possible stress tensors that are acceptable at 68% or 95% confidence level.

simple mathematical error model following *Brillinger et al.* [1980] (Appendix A) to account for increased misspick rate near nodes (equation (A1)).

The second step calculates *S'* for a grid of possible stress models, utilizing equation (7), and finds the maximum such score, *S*<sub>max</sub>. Differences between each *S'* and *S*<sub>max</sub> form the basis for assigning confidence limits to stress.

**2.3.1. Confidence limits.** As defined above, the scores *S'* have standard normal distribution with unit variance. This allows confidence limits to be estimated directly from a probability density function (pdf) for all parameters, or any subset of them [e.g., *Tarantola*, 1987]. We calculate the pdf over a grid of values for the four stress parameters *P*( $\Theta$ ,  $\Psi$ ,  $\Phi$ , and *R*), based on the normal distribution appropriate for such a sum of Bernoulli trials:

$$P(\Theta, \Psi, \Phi, R) = a \exp\{-\frac{1}{2} [S_{\max} - S'(\Theta, \Psi, \Phi, R)]^2\}, \quad (9)$$

where the constant *a* is chosen such that the integral of *P* over all parameter space is unity. In principle, the confidence region in this four-dimensional parameter space would be determined by finding the volume over which the integral of *P* gives the desired confidence level. In practice, only the relevant marginal confidence limits are presented, as discussed below.

In addition to confidence limits we also list the percent of stress tensors for which *S'* lies within the 68% and 95% confidence limit of the “best” score. While the listed percentages in Table 1 (“Acceptable Stresses”) may seem small compared to the bounds on axes on figures, it must be remembered that there are four stress parameters and each axis is defined by only two of them. Thus, while the 95% confidence bounds in  $\sigma_1$  may give 20-30° uncertainties, or include 10-15% of all possible orientations, these correspond to a subset of values for *R* or  $\sigma_3$  orientation and so correspond to only 3-5% of all possible stress tensors.

**2.3.2. Marginal Confidence Limits.** It is usually more convenient to examine one or two of the four parameters at a time, for example, the single value of *R* or the two angles ( $\Psi$ ,  $\Theta$ ) that define a particular principal stress axis orientation. This is done in all presented results by calculating marginal pdf's for the parameters of interest by numerical integration. For example, marginal confidence limits in location of stress axes are determined by numerically integrating the pdf (9):

$$P_{\text{axis}}(\Psi, \Theta) = \iint_{R, \Phi} P(\Psi, \Theta, \Phi, R) dR d\Phi \quad (10)$$

and then contouring areas that contain 68% and 95% of the

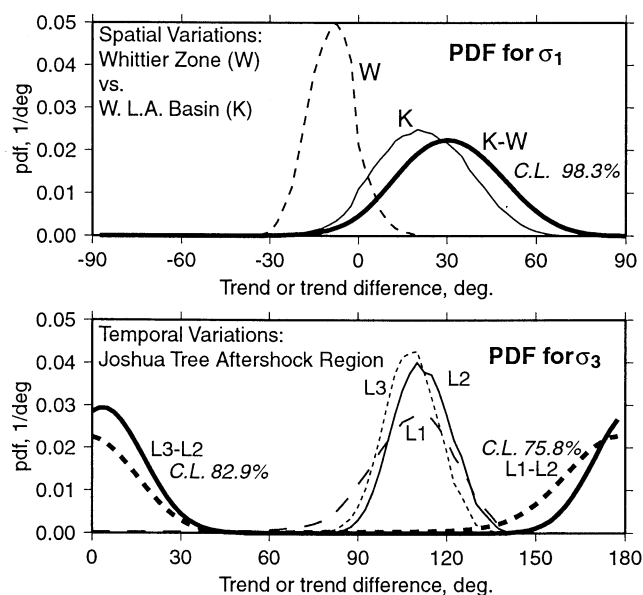


**Figure 4.** Comparison of marginal probability density functions (pdf's) for trend in a principal stress axis, among (top) two spatially adjacent clusters and (bottom) three temporally successive clusters in the same location. Spatially adjacent clusters, west Los Angeles Basin and Whittier aftershocks, correspond to clusters K and W on Table 1, while the temporally successive clusters correspond to L1, L2, L3, near the 1992 Joshua Tree earthquake. Thin lines indicate marginal pdf's for trend, calculated through numerical integration of pdf's as described in text; thick lines indicate pdf's for the difference in trend between sequential populations; "C.L." is largest confidence level at which each trend difference significantly deviates from 0°. The 33.3° difference in trend of  $\sigma_1$  between K and W is significant at 98.3%. The  $\sigma_3$  trend differences between the Joshua Tree aftershocks and prior seismicity (L1-L2) or later Landers aftershocks (L3-L2) are 1.4° and 5.9°; these trend differences are not significant at confidence levels above 75.8% and 82.9%, respectively.

resulting probability. Those areas are chosen to include the grid points with the largest marginal probability density, thus representing the confidence limits covering the smallest area. This procedure is somewhat different from that used in the FMSI compilation diagrams [Gephart, 1990b], which essentially show one- or two-dimensional projections of the four-dimensional confidence limits and therefore tend to slightly overestimate confidence regions.

**2.3.3. Hypothesis testing: Stress heterogeneity.** In addition to determining confidence limits on stress this approach provides a natural means of testing the significance of stress homogeneity. Formally, we test the null hypothesis ( $H_0$ ) that the focal mechanisms determined via MOTSI fit first motions equally well as ones determined without regard to stress, via MOTSI-FP which generates an aggregate score  $S_0$  that is calculated following (7). Rejecting  $H_0$  is a strong indicator of stress heterogeneity because such rejection indicates that the stress constraint significantly degrades fits. While an exact test could not be found, owing to the complex form of  $S$  (equations (6)-(7)), we give a close approximation for comparing simple binomial scores. The homogeneity hypothesis  $H_0$  can be rejected at confidence level  $1 - \beta$  when

$$dS = (S_0 - S_{\max}) > Z_\beta \sqrt{2} \quad (11)$$

where  $Z_\beta$  is the standard normal deviate at confidence level  $\beta$ . For each inversion the statistic  $dS$  is estimated as is the confidence limit  $\beta$  at which  $dS$  is significant (Table 1). The test is one sided because  $S_0 \geq S_{\max}$  always; the  $\sqrt{2}$  accounts for the pooled variance of the difference of two random variables based upon equal numbers of binomial observations [Larson and Marx, 1981]. Thus we reject the hypothesis  $H_0$  (and infer heterogeneous stress) at the 95% confidence level when  $dS > 2.32$  ( $Z_{0.95} = 1.64$ ). Values for  $dS$  of 1.0 and 2.0 then correspond to confidence levels of 76% and 92%, respectively.

**2.3.4. Hypothesis testing: Stress changes between populations.** Frequently, one is interested in the significance of apparent changes in stress two earthquake populations [e.g., Hauksson, 1994; Michael, 1987b; Seeber and Armbruster, 1995; Zhao et al., 1997]. Some insight can be gained from inspection of the marginal confidence limits of individual axes. In particular, if a best fitting principal stress axis of one population lies within the 95% confidence interval of that for a second population, stress for the two populations cannot be significantly distinguished at 95% confidence. The solution for the second population can always be changed to agree with the first without significantly violating data constraints.

A more rigorous test is needed in those cases where confidence limits overlap but best fitting stress estimates do not. Following Michael [1987b], we compare two populations, A and B, by test the significance of  $\theta_A - \theta_B$ , the rotation of the trend of a principal axis. The test proceeds as follows: (1) calculate the marginal pdf for stress axis for each of the two populations following equations (9)-(10) (chosen such that  $\theta_A > \theta_B$ ); (2) calculate the two marginal pdf's for  $\theta_A$  and  $\theta_B$  by numerically integrating the stress axis pdf's; (3) numerically calculate the pdf for  $\theta_A - \theta_B$ ,  $P_{A-B}$ , via the standard convolutional transform over the range  $-\pi/2$  to  $\pi/2$  [e.g., Apostol, 1969]; (4) integrate  $P_{A-B}$  from 0 to  $\pi/2$  to calculate the probability that  $\theta_A - \theta_B$  is greater than zero; and (5) reject the hypothesis that  $\theta_A = \theta_B$  if this integrated probability is greater than 95%.

Figure 4 shows two examples of such a test, one comparing  $\sigma_1$  orientations between two spatially adjacent regions in the Los Angeles Basin and one comparing  $\sigma_3$  for three temporally sequential data sets in the Landers region. In the former case, an apparent rotation of 33.3° is significant at any confidence level below 98.3%. In the latter case, a 5.9° rotation between the 1992 Joshua Tree aftershocks and subsequent Landers aftershocks (L3-L2) is not significant at the 95% confidence level, or any confidence level greater than 82.9%.

### 3. First Motion Data

In order to illustrate the utility of MOTSI, we use both synthetic data and real first motions from Southern California Earthquake Center (SCEC) catalog [Hafner et al., 1994], one of the largest catalogs of first motions available, with recordings of tens of thousands of events. Of the latter, we rely on events between 1981 and 1992, a time during which network operations were relatively stable.

Because we are aware of few guidelines in the literature for assessing uncertainties in first motions, we discuss our efforts here in evaluating the SCEC catalog. Data quality is generally evaluated by checking consistency of first motions to focal mechanisms, both those determined here (using MOTSI-FP described above) and those from the comprehensive determination of Seeber and Armbruster [1995]. While it would be



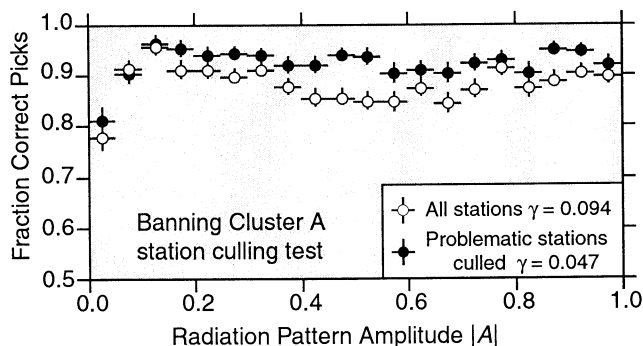


**Figure 5.** Improvement to data reliability by culling problematic stations. Data are from cluster A in the Banning Pass region. All events have  $\geq 20$  first motions at  $\leq 100$  km range and are at least 15 km deep. Unculled data (open circles) include all 67 recording stations, 223 events with 6050 picks. Those data indicate a misfit rate of 9.4% ( $\gamma = 0.094$ ). The culled data set (solid circles) has five problem stations removed, constituting 23% of the arrivals, and shows a 50% improvement in data quality ( $\gamma = 0.047$ ). Such improvement highlights the importance of eliminating data from chronically problematic stations.

preferable to compare first motions to focal mechanisms that are determined independently from them, we know of no sufficiently large focal mechanism compilations of small earthquakes that do not rely upon first motions. The following effects, many obvious, were found to significantly affect the quality of first motions:

1. Among all data there is a random probability ( $\gamma$ ) that a first motion is picked incorrectly regardless of focal mechanism [e.g., Aki, 1976]. We explicitly include a constant  $\gamma$  in estimating a priori uncertainties for each data set (equation (A1)).

2. Near-nodal arrivals are less reliable than others. This reliability is directly incorporated into the a priori uncertainties for each first motion by the parameter  $\alpha$  (Appendix A; see also Brillinger *et al.* [1980]). Our error model (equation (A1)) satisfactorily accounts for the frequency of mispicked polarities and its increase near nodes (Figures 5 and A1).

3. For local and regional observations, long paths provide less reliable first motions than short paths, presumably because long paths are either highly scattered within the crust or attenuated by refraction. In several tests we have observed that paths  $> 100$  km long are less likely to produce consistent first motions than short paths. While the effect could be included in  $p_{ij}$  estimates, we found it more practical to choose a cutoff distance beyond which rays are neglected, and following Seeber and Armbruster [1995], we utilize only those picks with corresponding ray paths  $< 100$  km long.

4. "Impulsive" arrivals are more reliable than those labeled "emergent." For several subsets of the SCEC data set, arrivals labeled emergent indicate a random picking error  $\gamma$  that is 0.2–1.0 times larger than for those labeled impulsive. Accordingly, we increase the assumed  $\gamma$  for emergent arrivals.

5. Network operating procedures change with time. As shown in Appendix A, the SCEC catalog shows relatively fewer inconsistencies after 1988 than before. The effect is minor, however, and no attempt is made to compensate for it.

6. A small number of stations are associated with many more polarity violations than others. These data dispropor-

tionately degrade the quality of the focal mechanisms (either with or without a stress constraint). For example, nine stations in southern California account for 28% of all polarity violations but only 9% of all picks. Some of these stations report violations for more than 50% of picks. We have rejected these data from our analyses; their inclusion would increase our estimate of  $\gamma$ , which would have the net effect of producing poorer constraints on stresses. The same stations reported inconsistencies for widely spaced event clusters, at varying ranges, so this effect is unlikely to be related to ray path. We cull such data separately for each studied cluster, by eliminating stations that report violation rates more than three standard deviations worse than the average misfit rate for that cluster. This procedure had the effect of increasing the fraction of consistent picks to 90–97% (e.g., Figure 5), greatly reducing the a priori estimates of  $\gamma$  and consequently reducing the size of confidence limits.

7. Events with poorly constrained focal mechanisms, either from insufficient or clustered first-motion observations, generally are not useful in constraining the stresses. For each event the quality of the focal mechanism is gauged by a statistic  $F_j$ , defined as the percent of gridded focal mechanisms that are not significantly worse than the best one at the 95% confidence level (i.e., the  $S_j$  are within 1.64 of the best score  $S_{j(\max)}$ ); events with low  $F_j$  are relatively well-constrained. We have found that inversions for stress that include many events with high  $F_j$  do not generate narrower confidence limits than inversions with fewer but better constrained events. This result is unfortunate, as MOTSI provides a potential tool for utilizing first motions from otherwise poorly constrained events. Typically, only events with  $F_j < 5$ –10% produce satisfactory results.

## 4. Results

### 4.1. Inversions of Artificial Observations

A series of tests, conducted with synthetic first motions, elucidate some of the properties of MOTSI. A suite of 17 noise-free focal mechanisms, each with 15 noise-free first motions, is generated so as to match a single stress model (Figure 2b). If the data are assumed to be perfect, the technique correctly identifies the stresses used to construct the data. In a series of inversions (Figures 6a–c) the estimated noise parameters  $\gamma$  and  $\alpha$  are varied to test their impact; the best fitting stress models remains essentially the same but the breadth of the error bounds varies. This indicates the importance of accurately assessing the quality of data a priori: In general, data assumed to be noisy will afford a poorer constraint on stress than data assumed to be accurate. These results underscore the need for evaluating and reducing data noise.

When the number of first motions is doubled to 30 per event, the error bounds shrink substantially (Figure 6d). As expected, better constrained mechanisms will aid in constraining stress (unfortunately, such well-sampled mechanisms are often unavailable). Finally, the addition of random noise to the first motions (Figure 6e) or focal mechanisms (Figure 6f) widens error bounds, as expected, but does not move the minima. In these cases, noisy data lead to polarity violations and reduced scores (compare  $S_{\max}$  listed in Figures 6b, 6e, and 6f). Overall, these tests demonstrate that MOTSI produces confidence limits that behave in reasonable ways in response to variations in data quality and the assumptions about it.



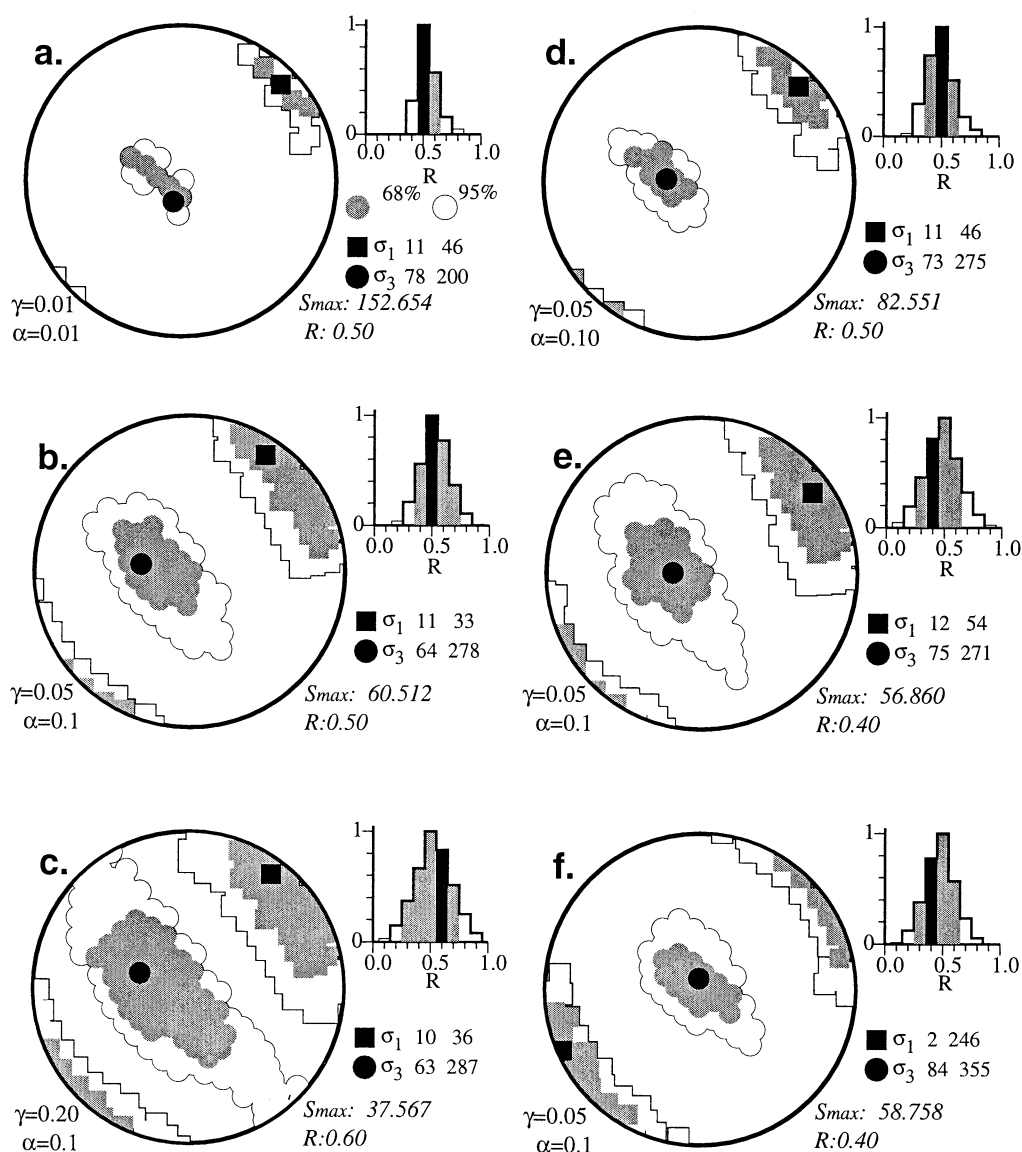


**Figure 6.** MOTSI results from inverting artificial data set. Data are 17 focal mechanisms with 15 first motions each, with rays and fault planes uniformly distributed and all first motions correctly assigned. Figure 2b shows the correct stress model used to generate slip vectors and first motions;  $R = 0.5$ . Inversion results with varying assumptions about the errors in the data, showing effect of assumed error model: (a) assuming near-perfect data,  $\gamma = \alpha = 0.01$ ; (b) assuming data accuracy typical of culled southern California data sets,  $\gamma = 0.05$  and  $\alpha = 0.1$ ; (c) assuming unusually noisy data,  $\gamma = 0.2$  and  $\alpha = 0.1$ . Note how confidence limits grow with increasing  $\gamma$ . (d) Inversion with increased data density of 30 first motions per event, resulting in smaller error bars. (e) Inversion with random noise added to first motions, with first motions inverted according to the a priori probabilities assumed ( $\gamma = 0.05$ ,  $\alpha = 0.1$ ). (f) Inversion with random noise added to focal mechanisms, rather than first motions, by a uniformly random rotation of up to  $60^\circ$ . In Figures 6d-6f, assumed error parameters are  $\gamma = 0.05$  and  $\alpha = 0.1$ . Format (MOTSI-Balls) is as follows: Circle shows lower-hemisphere equal-area projection of marginal confidence limits on  $\sigma_1$  and  $\sigma_3$  locations (squares and circles respectively). Solid shows best model, shaded and open regions show 68% and 95% confidence limits respectively. Top right shows marginal probability density function for  $R$ , with 68% and 95% confidence regions shown by shaded and open bars respectively. Also labeled are the best stress model described as plunge and trend for  $\sigma_1$  and  $\sigma_3$  (degrees),  $R$ , and  $S_{\max}$ .

#### 4.2. Example From Banning Pass, California

Many events near Banning Pass (Figures 7 and 8), just south of the “big bend” of the San Andreas Fault, are unusually deep among California earthquakes (to  $\sim 25$  km). Because of their depth and location within the southern California networks, they generate well-constrained focal mechanisms utilizing upgoing rays, which have small uncertainties in takeoff

angle. These data provide a useful illustration of our inverse approach. In order to avoid the effects of large events that occurred nearby in 1986 (North Palm Springs,  $M_w$  6.0) and 1992 (Joshua Tree,  $M_w$  6.2; Landers,  $M_w$  7.3; Big Bear,  $M_w$  6.5), we examine only those events from mid-1981 to June, 1986 and January, 1987 through March 1992 ( $M_w$  is moment magnitude from standard catalogs).

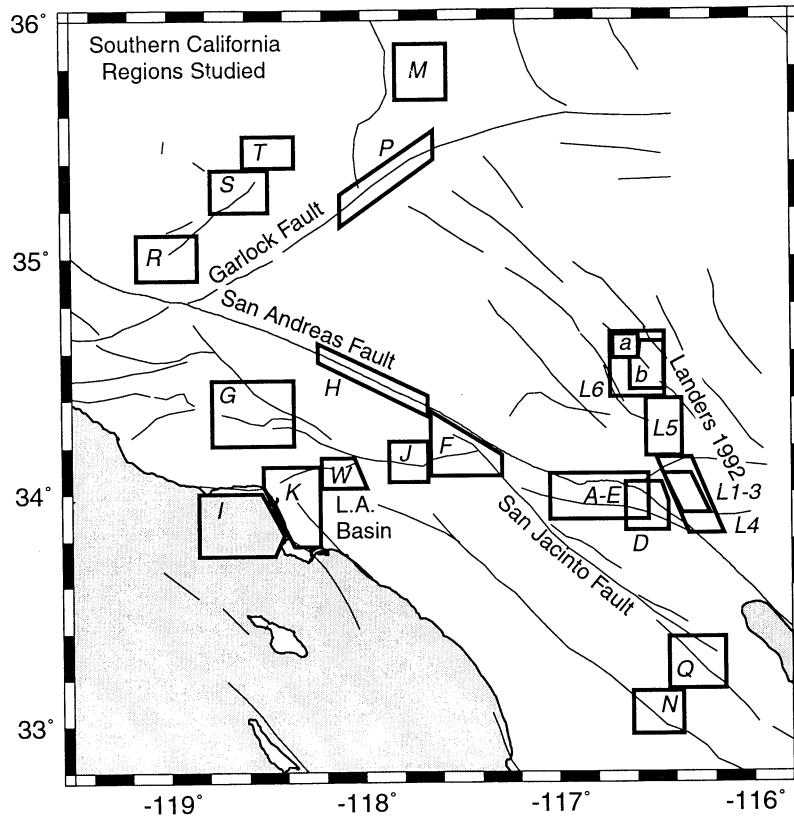


**Figure 7.** Map of southern California, showing major faults and regions selected for stress inversions. Letters correspond to ID in Table 1.

First motions (Figure 8) show variable sampling of the focal sphere and a small but fairly consistent number of polarity violations ( $>5\%$ ) after culling problematic stations (Figure 5). In this particular case, we restrict inversions to events with more than 20 first motions recorded at ranges of  $< 100$  km and well-constrained focal mechanisms (with  $F_j < 10\%$ , see section 3). Utilizing only events deeper than 15 km (hypocenters

of *Seeber and Armbruster* [1995]), these requirements yield a data set of 4657 first motions and 178 events (Table 1).

We performed parallel experiments on both compiled focal mechanism data (using FMSI [*Gephart, 1990b*]) and raw first motion data (using MOTSI). The best fitting stress models (Figure 9) of the two inverse techniques are similar and indicate N-S  $\sigma_1$  and E-W  $\sigma_3$ . These directions are generally con-

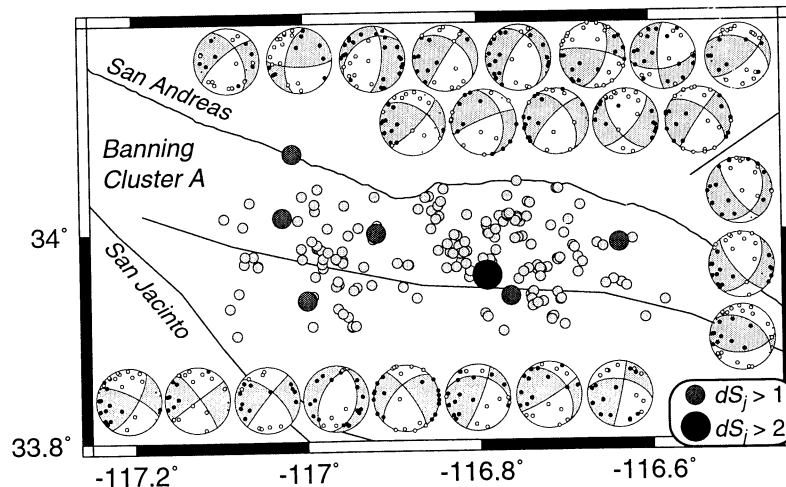


**Figure 8.** Map of event distribution in Banning pass region (labeled "A-F" on Figure 7), showing major faults, earthquake epicenters for cluster A, focal mechanisms, and first motions for select events. Arbitrarily selected focal mechanisms are lower-hemisphere equal-area stereonets, with compressional quadrants shaded and compressional arrivals solid. Solid circles on map denote events with large  $dS_j$  and hence increased probability of significant misfit due to imposing a homogeneous stress constraint;  $dS_j = 1$  and 2 correspond to 76% and 92% significance levels, respectively (equation (11)).

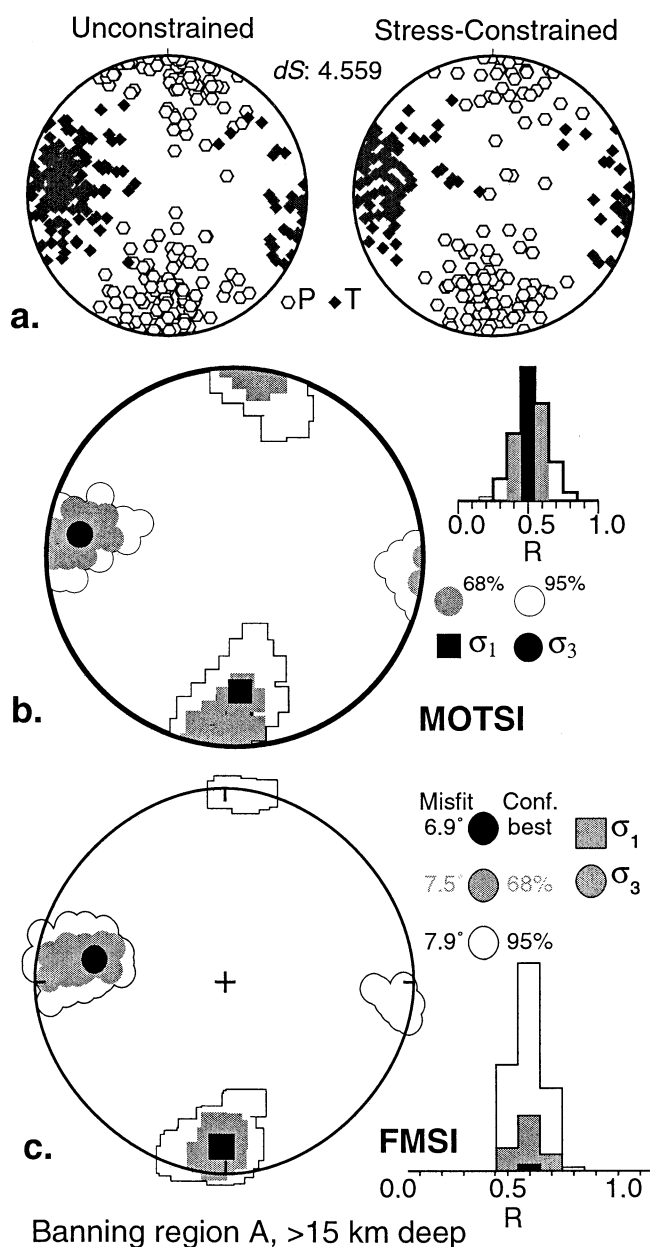


**Figure 9.** MOTSI results for deep events in the Banning Pass region (Table 1, cluster A) and comparison to FMSI results. (a)  $P$  and  $T$  axes for the 178 events used, as determined independently from (left) stress and (right) as part of MOTSI stress inversion. Note close similarity of the two distributions. (b) MOTSI stress inversion results. Format same as Figure 6. (c) Results from inversion of focal mechanisms (not first motions) using FMSI [Gephart, 1990b], provided for comparison. Focal mechanisms used here were those determined by MOTSI-FP (Left Figure 9a).

sistent with those found elsewhere in southern California, compiled and discussed below. The uncertainties here are somewhat larger than determined using other techniques, although the best stresses determined elsewhere lie within our 95% confidence limits (e.g., compare to *Seeber and Armbruster* [1995], who use the approach of *Michael* [1987a]).

The confidence limits determined by MOTSI appear only slightly larger than those determined by FMSI (Figure 9), suggesting that the main error source is well characterized by focal mechanism variation; this is not always the case. In actual-

ity, FMSI provides much smaller confidence limits; only 0.15% of possible stress tensors lie within the 95% four-dimensional confidence limit calculated by FMSI, as opposed to 0.66% calculated via MOTSI (Table 1). Because the MOTSI stress axis constraints are plotted as marginal confidence limits, discussed above, while FMSI plots a projection of the four-dimensional confidences [Gephart, 1990b], the resulting limits appear similar.

How much are the focal mechanisms degraded by the imposition of the stress constraint? We compare the focal mechanisms determined by MOTSI (referred to as "constrained mechanisms," consistent with the best stress) with those determined by MOTSI-FP ("unconstrained mechanisms," with no stress constraint) in two independent ways. First, we compare the scores from equation (7) for the best constrained and unconstrained focal mechanisms ( $S_{\max}$  and  $S_0$ ,

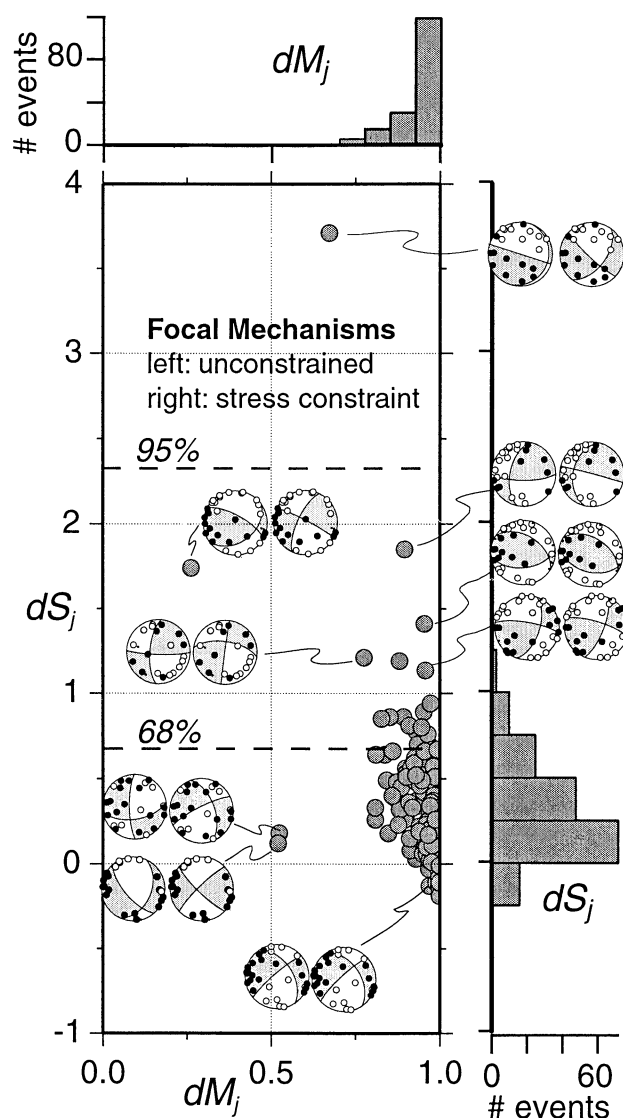


**Figure 10.** Changes to focal mechanisms for Banning Pass deep cluster A (Figures 8-9) induced by requiring homogeneous stresses. For all events, statistics illustrate change in mechanism ( $dM_j$ ) and change in fit to data ( $dS_j$ ). Dashed lines show confidence levels for which  $dS_j$  indicates degradation in fit due to imposing homogeneous stresses, for each event (equation (11)). Focal mechanisms show paired results for selected events, with unconstrained mechanism on left and stress-constrained mechanism on right.

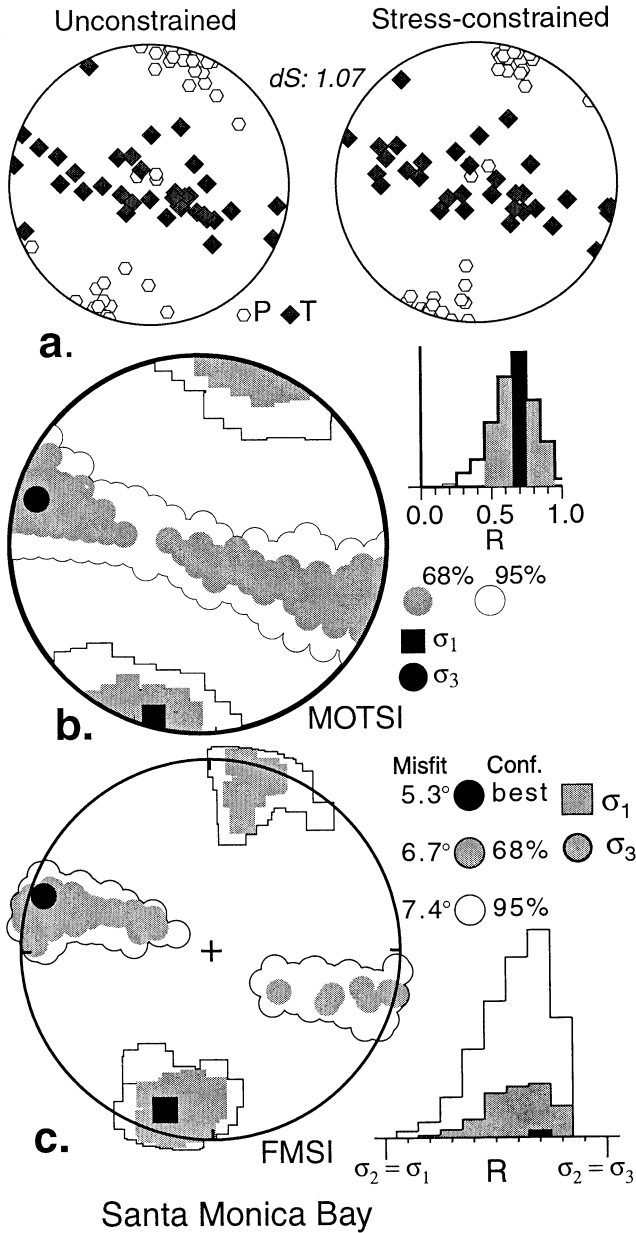


**Figure 11.** Stress inversion results for Santa Monica Bay. (a)  $P$  and  $T$  axes for constrained and unconstrained case. (b) MOTSI inversion result. (c) FMSI inversion result. Format same as Figure 9.

respectively), giving a score degradation  $dS$  following equation (11). Second, we consider the differences in orientation between the best constrained and unconstrained focal mechanism for event  $j$  using the statistic

$$dM_j = 0.5 \mathbf{M}_j : \mathbf{M}_j^c = 0.5 \sum_{kl} M_{jkl} M_{jkl}^c, \quad (12)$$

where  $\mathbf{M}_j$  and  $\mathbf{M}_j^c$  are the amplitude-normalized moment tensors for the unconstrained and constrained mechanisms, respectively, and ":" represents the tensor double inner product as shown. This statistic is 1.0 if the two mechanisms are identical and -1.0 if the mechanisms have the same nodal planes but opposite polarities. For double-couple mechanisms this reduces to

$$dM_j = 0.5 * [(\mathbf{p} \cdot \mathbf{p}^c)^2 + (\mathbf{t} \cdot \mathbf{t}^c)^2 - (\mathbf{p} \cdot \mathbf{t}^c)^2 - (\mathbf{t} \cdot \mathbf{p}^c)^2], \quad (13)$$

where  $\mathbf{p}$ ,  $\mathbf{t}$  and  $\mathbf{p}^c$ ,  $\mathbf{t}^c$  are unit vectors along the  $P$  and  $T$  axes for the two mechanisms.

For the Banning Pass test case, most of the constrained focal mechanisms were nearly identical to the unconstrained ones ( $dM_j$  in Figure 10). Likewise, the change in fit to first motions ( $dS_j$ , equivalent to  $dS$  for a single event) is relatively small in order to match the stress tensor. Only one event shows significant degradation of fit ( $dS_j > 2.32$ ; see equation (11)) and so may be inconsistent with the best fitting stress field. Twenty-three events have substantially different mechanisms ( $dM_j < 0.9$ ) without much difference in score ( $dS_j < 1.0$ ). For these events, first motions from these events are almost equally consistent with two different focal mechanisms, although only one of these is consistent with the best stress model.

The test statistic for the entire population ( $dS$  in Table 1) is significantly greater than zero (4.55), indicating that overall the hypothesis of homogeneous stress can be ruled out. However, it is not obvious that this poor fit reflects any large-scale

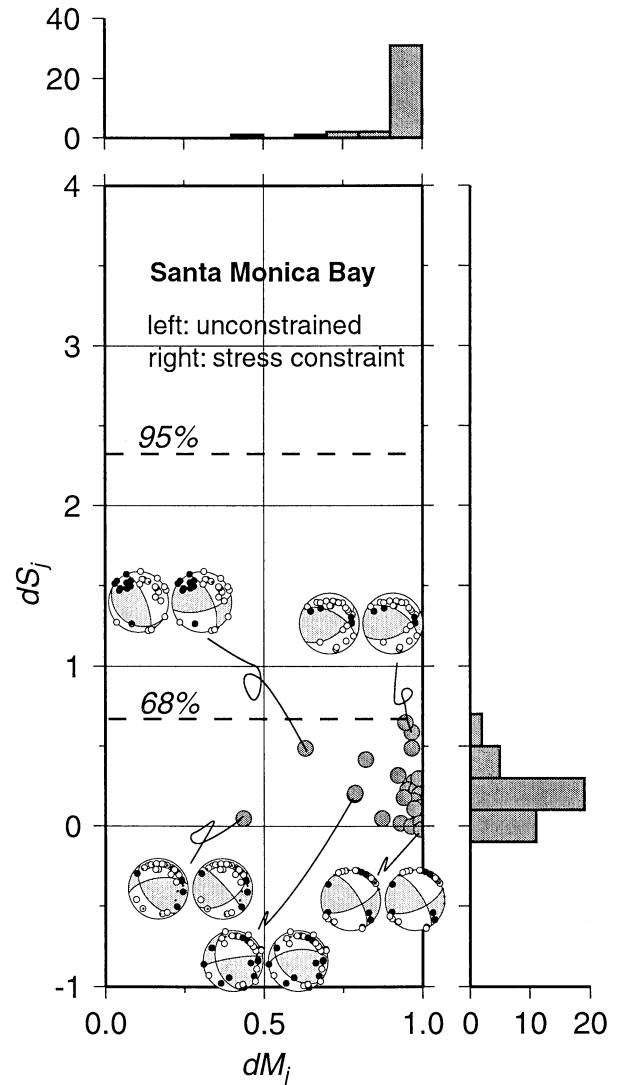


**Figure 12.** Changes to focal mechanisms ( $dM_j$ ) and increased misfit ( $dS_j$ ) for Santa Monica Bay cluster (cluster I on Table 1), induced by requiring homogeneous stresses. Format same as Figure 10. While  $dS_j < 0.65$  for all events, indicating good fit, 4 of 37 events show noticeable change to mechanism ( $dM_j < 0.8$ ). A wide variety of focal mechanisms appear to be consistent with many of these events.

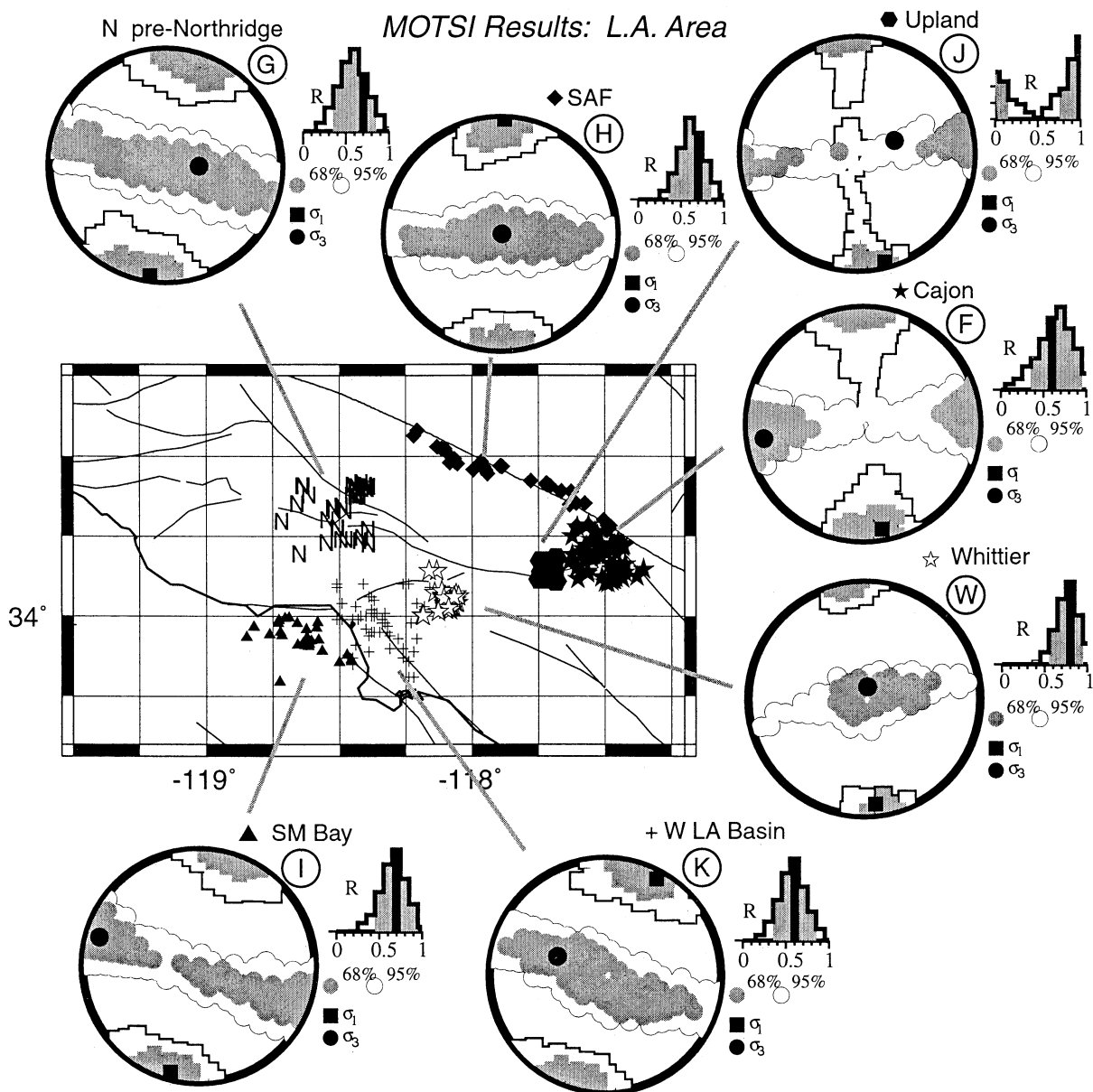


**Figure 13.** Results from MOTSI inversion for select clusters from the Los Angeles Basin area. Format of MOTSI balls is same as Figure 6. Regions correspond to clusters F-K and W in Table 1 and Figure 7 (circled letter).

spatial variations in stress, as events with high  $dS_j$  (e.g., Figure 10) are widely scattered across the region (Figures 8 and 10). Stress may vary over length scales too small to resolve from these data.

#### 4.3. Example From the Santa Monica Bay, California

Inversions of data for 37 events from the Santa Monica Bay region illustrate further differences between MOTSI and other approaches (Figure 11). These data provide a second, complementary example to the Banning Pass region, one in which ray path distribution is comparatively poor (the events are offshore and rays are all downgoing) and first motions show higher rates of inconsistency ( $\gamma = 0.079$ ). Here, MOTSI indicates that  $\sigma_1$  is NNE with  $35^\circ$  uncertainties (95% confidence limits) and  $\sigma_3$  is virtually unconstrained in a girdle around  $\sigma_1$ , consistent with a relatively high value for  $R$ . *Hauksson and*

*Saldivar* [1989] recovered a nearly identical stress constraint, including a high value for the parameter we call  $R$ .

From the low  $dS$  of 1.07 (Table 1) we cannot reject the null hypothesis that stresses are homogeneous at 95% confidence level, validating the uniform stress assumption. Few events show inconsistency with the best stress, indicated by  $dS_j < 0.65$  for all events (Figure 12). On the other hand, several mechanisms show  $dM_j$  far from 1.0 indicative of large changes in focal mechanism; 4 of 37 show  $dM_j < 0.8$ , as opposed to 5 of 178 for the Banning example. It appears that the requirement of homogeneous stresses here leads to changes in many mechanisms but not increased misfit, perhaps because the Santa Monica first motions offer less constraint.

The MOTSI confidence limits on stress are larger than indicated by FMSI, when the uncertainties in focal mechanism are fully taken into account (Figure 11). In particular, the FMSI inversion calculates confidence limits that are inconsistent

with a vertical  $\sigma_3$ . FMSI also estimates that 0.59% (0.15%) of all possible stress tensors lie within the 95% (68%) confidence limit, as opposed to 3.94% (0.62%) for MOTSI. The reason for the smaller FMSI confidence limits is unclear, but may result from the use of a more precise prescription of focal mechanisms than is warranted from the first motions. Because MOTSI is able to adopt different focal mechanisms consistent with the first motions, as required by certain stress models, it correctly recognizes the weaker constraint imposed by these first motions.

#### 4.4. Compilation of Southern California Stresses

We applied MOTSI to 27 groups of focal mechanisms from the southern California catalog with results shown in Table 1. The groups were defined by spatial and temporal clustering of events (Figure 7), including aftershock sequences, or by interesting patterns in stress suggested by previous work, and events are selected as described above. (We do not include the 1994 Northridge sequence owing to its complexity [e.g., *Gephart, 1998*]). For events occurring prior to December 1992 and south of 35.5°N, we use the relocated hypocenters and ray takeoff angles of *Seeber and Armbruster [1995]*, which are based on a variety of regionally appropriate one-dimensional models. Other events are relocated and ray angles are calculated using smoothed one-dimensional velocities based on the one-dimensional starting model of *Hauksson and Haase [1997]*. Reference focal mechanisms are determined using MOTSI-FP, for which the error rate parameter  $\gamma$  is estimated independently for each cluster (Table 1). Then, the first motions are inverted simultaneously for stresses and focal mechanisms using the  $\gamma$  estimates for each cluster. Results for regions around the Los Angeles Basin are shown in Figure 13, and all are listed in Table 1.

The groups tested include varying numbers of events, from 36 to 200, and yield varying estimates of  $\gamma$  (Table 1). High values of  $\gamma$  reflect noisier than usual first motions and tend to produce broader confidence regions for stress than others. For example, the west Los Angeles Basin events exhibit unusually noisy first motions ( $\gamma = 0.092$ ) and provide a weak constraint on stress (Figure 13). By contrast, the deeper Banning Pass events (Figure 9) exhibit less noisy first motions ( $\gamma = 0.058$ ) and provide a stronger constraint.

In nearly all cases, the imposition of a constant stress on a cluster did not result in large degradation of fit as indicated the  $dS$  heterogeneity test and the corresponding confidence limit for which the homogeneous stress hypothesis can be accepted ("Significance" in Table 1). Values for  $dS > 2.32$ , corresponding to a nominal 95% confidence limit in the stress heterogeneity test (equation (11)), occur rarely, only in the Deep Banning Pass cluster, events in the Coso geothermal area, and in several aftershock sequences. Also,  $dS$  never exceeds 4.6 among the tests shown, with the important exception of cluster L6 (see section 5.2). Hence, in most cases the first-motion data are consistent with a locally homogeneous stress field, at least at times when local transients are unlikely.

On a case-by-case basis, our results are broadly consistent with most previous stress inversion studies in southern California, which show an overall tendency for  $\sigma_1$  oriented N-S [e.g., *Jones, 1988; Hauksson and Saldivar, 1989; Hauksson, 1990; Michael, 1991; Hartse et al., 1994; Castillo and Zoback, 1995; Seeber and Armbruster, 1995*]. However, generally, we do not support interpretations of subtle local spatial or

temporal variations in stress based on detailed data segregations (see section 5.1), and stress rotations of a few degrees do not seem constrainable with this sort of data. In virtually all of the studied clusters (e.g., Figure 13), rotations of 20–30° could be applied to the best fitting stress tensor without significantly violating the first-motion data (e.g., Figure 4). We submit that realistic uncertainty estimates, which incorporate meaningful uncertainties in focal mechanisms, do not permit us to resolve small variations in stress (e.g., < 20–30°), at least not with the routine seismicity catalog data analyzed here. These uncertainties are a direct result of the finite probability  $\gamma$  that a given first motion will be incorrectly predicted by any focal mechanism and of incomplete sampling of the focal sphere by  $P$  waves.

## 5. Discussion

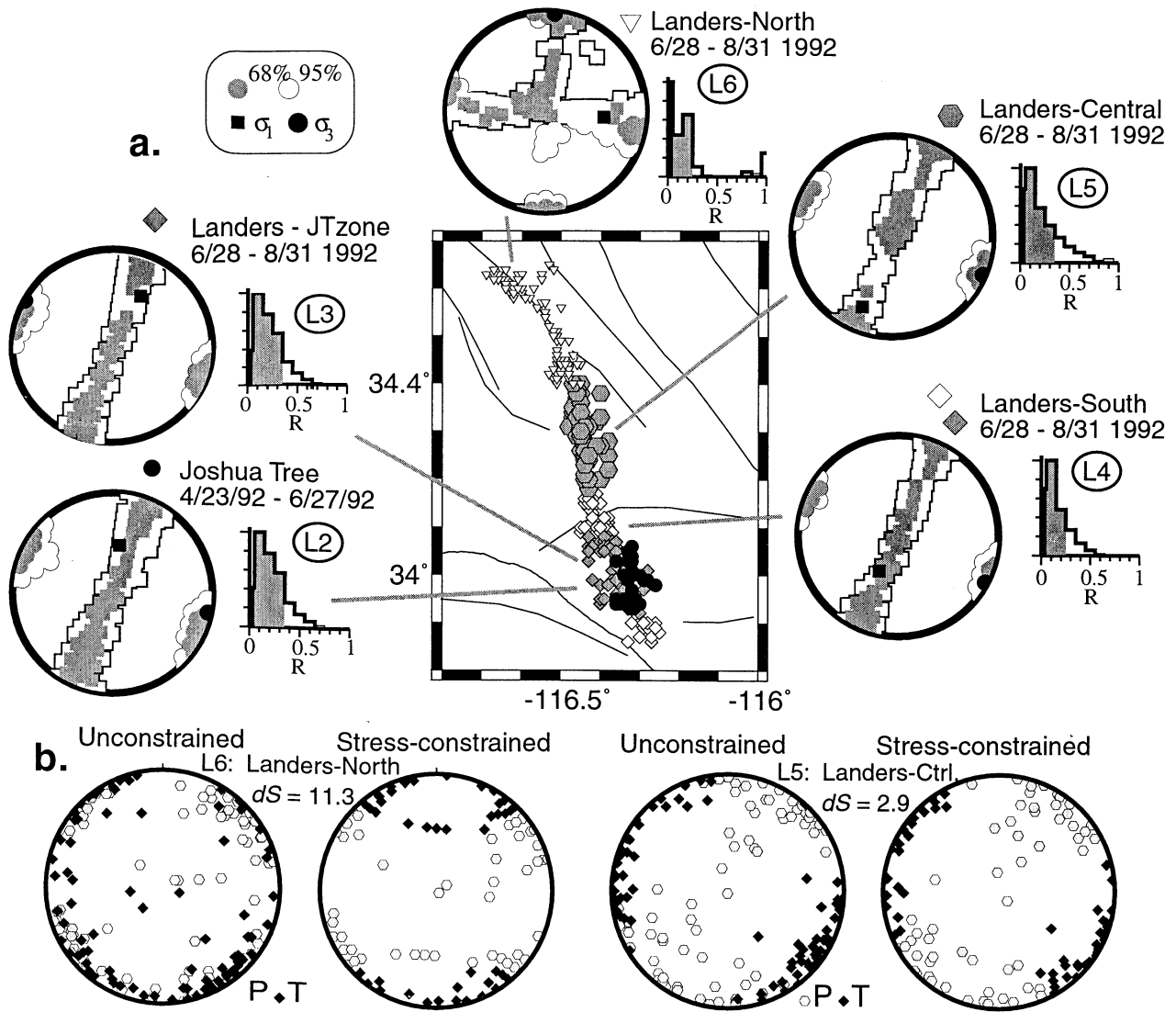
### 5.1. How Good Are Stress Constraints?

As discussed above, even for the best clusters, it is unlikely that principal stress axis orientations can be constrained to within 20–30° if uncertainty in focal mechanisms is taken into account. The primary source of the uncertainty seems to be noise in first motions, quantified as  $\gamma$ , which is everywhere > 0.03 (suggesting 3% polarity violations, independent of radiation pattern). In particular, temporal stress rotations of 5–15° suggested elsewhere [*Zhao et al., 1997; Hauksson, 1994*] may not be resolvable unless unrealistic confidence is assigned to the focal mechanisms. Figure 1 illustrates one way in which this might happen with traditional stress inversions, as variability in mechanism induced by data noise produces the apparent fault plane diversity needed to constrain stresses. The most obvious way to improve the critical picking statistics is to improve the quality of the first motions, such that they are more consistent with focal mechanisms. The study of *Zhao et al. [1997]* on the Northridge sequence made use of rays traced in a three-dimensional velocity structure which conceivably have sufficient reliability to provide the smaller error bounds needed (however, they do not follow our error analysis). Alternatively, inverse techniques based on focal mechanisms determined by other means (such as by waveform inversion) may provide better stress constraints.

### 5.2. Northern Landers sequence: No Consistent Stresses

The MOTSI inversions provide a useful way to identify those regions for which a homogeneous stress is demonstrably not consistent with first motions, so we close with a discussion of one such region. A deviation from homogeneity of  $dS = 11.27$  is calculated for the north segment of the Landers ( $M_w = 7.3$ ) aftershock sequence (cluster L6), significant at confidence levels in excess of 99.99%. Likewise, previous studies [*Hauksson et al., 1993; Hauksson, 1994*] suggested the occurrence of stress perturbations here associated with the Landers main shock. Stresses are inverted separately for the southern, central, and northern part of the Landers aftershock sequence for the 2 months following the June 28, 1992 main shock (Figure 14). In addition, we invert aftershocks of the April 22, 1992 Joshua Tree event that occurred prior to Landers, as the two aftershock zones overlap. In general, the quality of data is high ( $\gamma = 0.040$ – $0.075$ ).

For many of these tests (L2–L5), a common well-constrained stress tensor (with narrow confidence limits) was found that agreed with the first motions ( $dS = 1.48$  to 2.88;



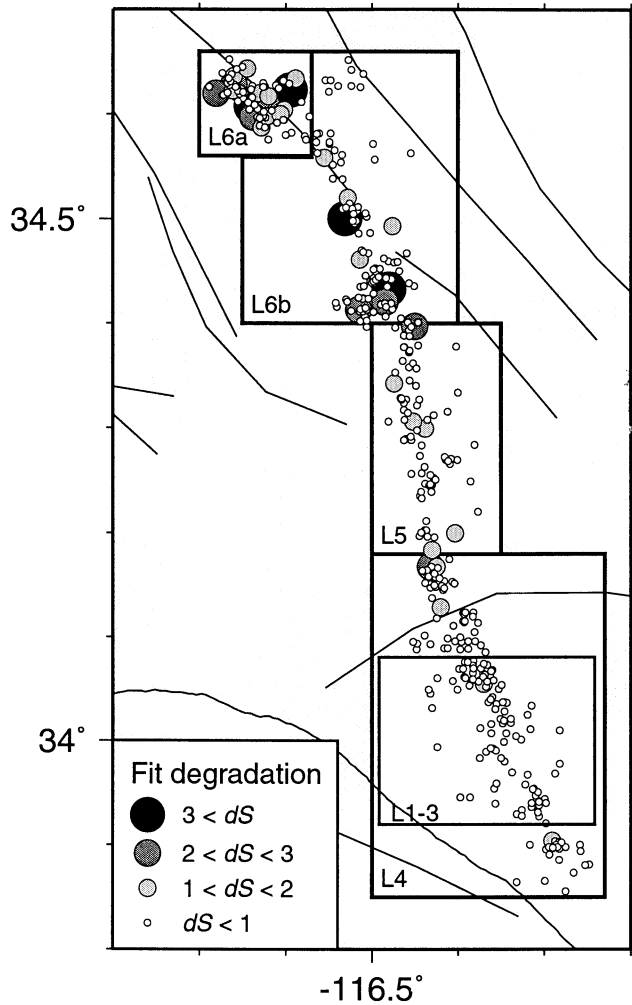
**Figure 14.** (a) Results from inverting Landers and Joshua Tree aftershock clusters. Format same as Figure 6. (b)  $P$  and  $T$  axis orientations for two Landers clusters, illustrating the effects of imposing the uniform stress constraint within each cluster. Format is the same as Figure 9a. Note scatter of Landers north mechanisms.

Figure 14). That these three stress tensors are nearly identical to one another (Figure 4) suggests that a single stress field may account for most of the slip along much of this fault. Although  $dS = 2.63$  and  $2.88$  for regions L4 and L5, formally inconsistent with a homogeneous stress field at the 95% confidence level, the similarity of all inversion results suggests that small local stress heterogeneities may influence small numbers of events; inspection of Figure 15 reveals that one such region lies at a fault step near the L4-L5 box boundary. For example, we see no evidence for a  $\sim 14^\circ$  temporal rotation of stresses between the two southern clusters (Joshua Tree, L2, and southern Landers aftershocks, L3 or L4), as previously argued by Hauksson [1994] based on the method of Michael [1984, 1987a] (Figure 4). Given the width of any of the individual pdf's in trend of  $\sigma_3$ , stress rotations would need to be at least  $20^\circ$  before they would be significant. Effects of uncertainties among the focal mechanisms appear to be larger than previously recognized.

At the northern end of the Landers aftershock zone (near the Camp Rock Fault) estimated  $dS$  values are inconsistent

with homogeneous stresses at confidence levels  $> 99.99\%$  (cluster L6). We tested the possibility that this is a result of spatial variations in stress by subdividing the northern region into two clusters but still achieved a very poor fit ( $dS > 7.8$  for the northern segment L6a alone). Although stresses must be homogeneous at some small scale, repeated subdivision of the L6 cluster could not identify that scale. To illustrate the problem, in Figure 15 we show a map view of  $dS_j$  values for all events used in the several Landers inversions, in each case relative to the local stress determined. Along the southern two thirds of the fault zone, nearly all events are consistent with a stress model that is regionally homogeneous. However, nearly half of the events in the northern region are not, with extreme values of  $dS_j$ . The most reasonable explanation in our view is that the stresses that generated these earthquakes are heterogeneous, consistent with the interpretation of Hauksson [1994]. This condition may reflect near total stress drop associated with the main shock rupture, relieving large-scale stresses near the rupture surface and leaving only residual, disorganized perturbations. A similar situation was inferred from early af-





**Figure 15.** Map showing  $dS_j$  variations along the Landers fault zone. Symbol size and shading scales to  $dS_j$ , showing increased misfit due to enforcing homogeneous stress within each box.  $dS = 1, 2$ , and  $3$  correspond to 76.0%, 92.1%, and 98.3% significance levels of misfit, respectively (equation (11)). Note that many events in the northern end of the fault zone cannot be fit with a locally homogeneous stress model. We do not observe this property among any other data set in southern California.

tershocks at the northwest end of the Loma Prieta rupture zone [Michael *et al.*, 1990; Gephart, 1997], which indicate poorly constrained stresses varying in spatial subdomains, but everywhere nearly parallel or perpendicular to the main shock rupture zone.

## 6. Conclusions

We have developed a new method for estimating stresses from earthquake observations that inverts directly the  $P$  wave first motions commonly used to determine focal mechanisms. Unlike most previous strategies, our method (MOTSI) is fully nonlinear and provides more complete uncertainty assessments of the results. The uncertainties reflect both the real variation in fault geometries (as indicated by focal mechanisms) and the distributions of, and errors among, the first motions of each mechanism. As a consequence, our confidence limits are somewhat larger than obtained by others but are generally rea-

sonable. The approach also provides a natural test for heterogeneity within a population, expressed as the statistic  $dS$ , which indicates rejection of the homogeneous stress hypothesis when it exceeds 2.32 (95% confidence level).

In order to achieve accurate estimates of stress it is necessary to have well recorded events (each with, say, more than 20-30 first motions) with few polarity violations (say,  $\gamma < 0.05$ ). For real data sets we find uncertainties in stress orientations typically to be 20-30° or more. Hence many small stress variations of 20° or less previously inferred by others may not be resolvable with catalog data, as used here.

Application of MOTSI to 27 clusters of earthquakes across southern California has indicated that stresses are generally homogeneous within each group and, to a first order, across the whole region. This is quantified by the observation that over each population, there is only a small difference ( $dS$ ) between  $S_0$ , the fit of the first motions to the best focal mechanisms and  $S_{max}$ , the fit of the first motions to stress-consistent focal mechanisms. For many individual events the best fitting focal mechanisms determined with and without a stress constraint differ ( $dM_j < 1$ ), but the difference in the degree of fit to the first motions is not significant ( $dS_j$  remains small).

The largest violations of heterogeneity lie at the north end of the Landers sequence. That L6 group of aftershocks is not consistent with any homogeneous stress field and, as suggested by others, may be a site where stresses were significantly altered by faulting. Other aftershock sequences also fail the formal test for stress homogeneity ( $dS > 2.32$ ), perhaps reflecting the tendency toward locally significant stress changes associated with large earthquakes. In conclusion, MOTSI is a rigorous tool for evaluating stress from  $P$ -wave first motion data and can be used to identify those regions and events that show anomalous stress patterns.

## Appendix A: Estimated Picking Uncertainties and Comparison With Southern California Observations

The southern California first-motion data set provides a wealth of opportunity to test models of the error process associated with first-motion focal mechanisms. We use these data,

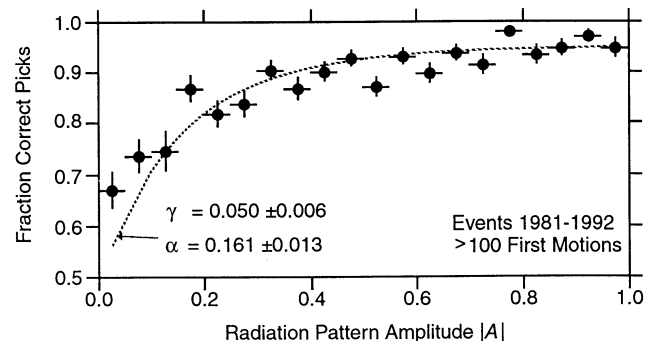


**Figure A1.** Consistency of first motion picks with focal mechanisms. First motions are taken from SCEC catalog, 1982-1992, for the 34 events that generate at least 100 first motions, constituting 4025 picks. Reference focal mechanisms are determined without regard to stress, as described in text. The variation the consistency of first motions with radiation patterns is then inverted to determine the two parameters of the error model  $\gamma$  and  $\alpha$  (equation A1), giving results shown.

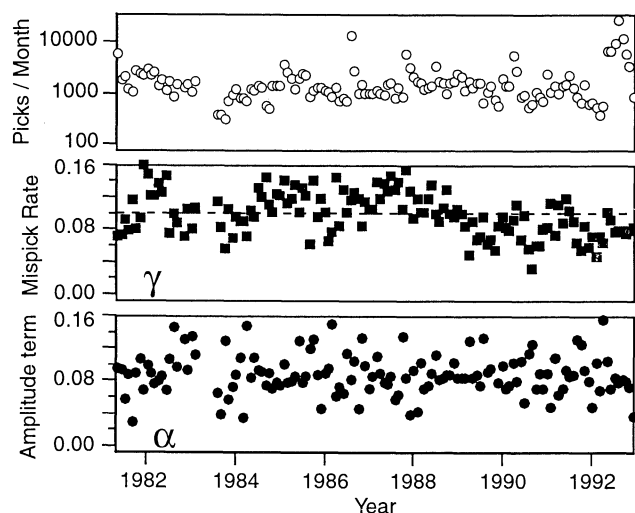


**Figure A2.** Estimates of first-motion error rate parameters  $\gamma$  and  $\alpha$  for each month in the SCEC catalog. First-motion data include all events generating at least 25 first motions, 1981-1992. These are compared to the focal mechanisms of *Seeber and Armbruster* [1995]. Note relative constancy of parameters with time and similarity to estimates on Figure A1 and Table 1, which utilize a different scheme for determining focal mechanisms.

together with the focal mechanism solutions of *Seeber and Armbruster* [1995] and additional ones generated in this study (that are independent of stress constraints), to assess the probability  $p$  that a first-motion pick will be correct. For a set of  $N$  (binomial) picks within the same data class (i.e., with the same probability  $p$  of being correct), an unbiased estimator for  $p$  is  $L/N$ , where  $L$  is the number of correct picks. Our procedure for estimating  $p$  is (1) to select representative data subsets, (2) to compare the observed picks to those predicted for our best estimates of focal mechanisms, (3) to calculate  $L/N$  for each data class from the histograms generated, and (4) to fit these estimates to an error model that describes variation between data classes. Typically, histograms are generated for different values of radiation pattern amplitude  $|A|$  with 20 evenly spaced bins in  $|A|$  (e.g., Figure A1).

The histograms constrain two parameters,  $\gamma$  and  $\alpha$ , which characterize the probability of correct picks as a function of radiated amplitude;  $\gamma$  is the random probability that a first motion picked incorrectly regardless of focal mechanism, and is the simplest measure of data quality. Typically, we expect  $\gamma$  to be  $< 0.5$  (i.e., first motions are usually of the correct polarity), although *Aki* [1976] has shown instances for which that is not the case. The estimate of  $p$  is parameterized by [e.g. *Brillinger et al.*, 1980]

$$p = \gamma + (1 - 2\gamma)[1 - 0.5 e^{-|A|/\alpha}] \quad (\text{A1})$$

(equivalent to  $p_{ij}$  in the main text), where  $A$  is the radiation pattern amplitude (0 at nodes,  $\pm 1$  at the  $P$  and  $T$  axes);  $\alpha$  is a characteristic amplitude below which a first-motion polarity is much more likely to be incorrect. For nodal arrivals,  $A = 0$  and  $p = 0.5$ , while for  $|A|$  near 1.0,  $p$  approaches  $(1 - \gamma)$ . This empirical form is very similar to the statistical model presented by *Brillinger et al.* [1980]. It also does a reasonable job of explaining data (Figure A1), although in our experience the value of  $\alpha$  predicted from data depends to some degree on the procedure used to determine reference focal mechanisms.

In practice we assign  $\alpha = 0.1$ , consistent with the observation that rays within  $5\text{--}10^\circ$  of nodal planes are much more likely to indicate polarity violations than other rays. Experience with ray tracing suggests that typically, it is difficult to fit all first motions within  $5\text{--}10^\circ$  of the nodal planes, or when  $|A| < 0.05\text{--}0.1$ . As shown in Figure A1, the best recorded events from the SCEC catalog (34 events, with  $>100$  first-motion picks at stations within 100 km) collectively indicate a value near  $\alpha = 0.1$ . With this large number of arrivals per event we find that the shape of the histogram is not strongly dependent on the procedure for generating focal mechanisms. Similar tests, utilizing focal mechanisms independently determined by *Seeber and Armbruster* [1995], also give  $\alpha$  values near 0.1 (Figure A2).

To test temporal stability of the  $p$  estimates, we construct histograms for the southern California data set, independently for each month from 1981 to late 1992 (Figure A2). These tests compare the southern California first-motion data set (for events with  $> 25$  first motions) to the focal mechanisms of *Seeber and Armbruster* [1995]. From this "unculled" data set (i.e., without rejecting unreliable stations) we find that values of  $\gamma = 0.08\text{--}0.12$ , or 8-12% mispicks, characterize most of the data subsets. This value appears to decrease slightly around 1988 (Figure A2, top), perhaps reflecting improvements in network operating procedures. This estimated  $\gamma$  is somewhat larger than assumed in our final inversions because we remove several chronically problematic stations.

**Acknowledgments.** J. Armbruster and L. Seeber provided the initial relocated data set for southern California. Additional data were provided by the Southern California Earthquake Center (SCEC) Data Center, mostly from the Southern California Seismic Network. We acknowledge operators of the Caltech and USGS seismic networks who make all of these data available. The manuscript benefited from thorough reviews of A. Michael, M. Zoback and R. Harris. Some plots are created using GMT [Wessel and Smith, 1991]. This work funded through USGS grants 1434-94-G-2439 and 1434-HQ-96-GR-2728 (GA), and USGS 1434-94-G-2412 and 1434-HQ-96-GR-2719 (JG).

## References

- Abers, G.A., and J.W. Gephart, Constraining the regional stress tensor directly from seismic first-motion observations, *Proc. Int. Union Geol. Geophys. Gen. Assembly XXI*, B339, 1995.
- Abers, G.A. and J.W. Gephart, Stress variations in southern California determined by direct inversion of seismic first motions (MOTSI), *Eos Trans. AGU*, 78(46), Fall Meet. Suppl., F451, 1997.
- Aki, K., Signal to noise ratio in seismic measurements, in *Volcanoes and Tectonosphere*, edited by K. Aoki and S. Iizuka, pp. 187-192, Tokai Univ. Press, Tokyo, 1976.
- Anderson, E.M., *The Dynamics of Faulting*, 206 pp., Oliver and Boyd, White Plains, N.Y., 1951.
- Angelier, J., Tectonic analysis of fault slip data sets, *J. Geophys. Res.*, 89, 5835-5848, 1984.
- Apostol, T.M., *Calculus*, vol. II, *Multi-variable Calculus and Linear Algebra, With Applications to Differential Equations and Probability*, 2nd ed., 673 pp., John Wiley, New York, 1969.
- Baumgardner, J. R., and P. O. Frederickson, Icosahedral discretization of the two-sphere, *SIAM J. Numer. Anal.*, 22, 1107-1115, 1985.
- Bott, M. H. P., The mechanics of oblique slip faulting, *Geol. Mag.*, 96, 109-117, 1959.
- Brace, W.F., and D.L. Kohlstedt, Limits on lithospheric stress imposed by laboratory experiments, *J. Geophys. Res.*, 85, 6248-6252, 1980.
- Brillinger, D.R., A. Udias, and B.A. Bolt, A probability model for regional focal mechanism solutions, *Bull. Seismol. Soc. Am.*, 70, 149-170, 1980.
- Castillo, D.A., and M.D. Zoback, Systematic stress variations in the

- southern San Joaquin Valley and along the White Wolf fault: Implications for the rupture mechanics of the 1952 *Ms* 7.8 Kern County earthquake and contemporary seismicity, *J. Geophys. Res.*, **100**, 6249-6264, 1995.
- Dillinger, W.H., S.T. Harding, and A.J. Pope, Determining maximum likelihood body wave focal plane solutions, *Geophys. J. R. Astron. Soc.*, **30**, 315-329, 1972.
- Gephart, J. W., Stress and the direction of slip on fault planes, *Tectonics*, **9**, 845-858, 1990a.
- Gephart, J. W., FMSI: A FORTRAN program for inverting fault/slickenside and earthquake focal mechanism data to obtain the regional stress tensor, *Comput. Geosci.*, **16**, 953-989, 1990b.
- Gephart, J. W., Spatial variations in stress from the first six weeks of aftershocks of the Loma Prieta earthquake, in *The Loma Prieta, California Earthquake of October 17, 1989*, edited by P. Reasenberg, *U. S. Geol. Surv. Prof. Pap.*, **1550**, D73-D89, 1997.
- Gephart, J. W., Investigating spatial variations in the state of stress from ten weeks of aftershocks of the Northridge earthquake, paper presented at NEHRP Conference and Workshop on Research on the Northridge, California Earthquake of January 17, 1994, Calif. Univ. for Res. in Earthquake Eng., Richmond, Calif., 1998.
- Gephart, J.W., and G.A. Abers, Estimating the regional stress tensor from seismic first motion observations: Uncertainty in focal mechanisms and the importance of error-free data, *Eos Trans. AGU*, **77**(46), Fall Meet. Suppl., F518, 1996.
- Gephart, J. W., and D. W. Forsyth, An improved method for determining the regional stress tensor using earthquake focal mechanism data: Application to the San Fernando earthquake sequence, *J. Geophys. Res.*, **89**, 9305-9320, 1984.
- Guinn, S.A., and L.T. Long, A computer method for determination of valid focal mechanisms using P wave first motions, *Earthquake Notes*, **48**, 21-33, 1977.
- Hafner, K., R.W. Clayton, and E. Hauksson, Archive of seismological data at the SCEC Data Center (SCEC DC), *Seismol. Res. Lett.*, **65**, 50, 1994.
- Hartse, H., R. C. Aster, M. C. Fehler, J. Scott, and F. Vernon, Evidence for small-scale stress heterogeneity in the Anza Seismic Gap, southern California, *J. Geophys. Res.*, **99**, 6801-6818, 1994.
- Hauksson, E., Earthquakes, faulting and stress in the Los Angeles Basin, *J. Geophys. Res.*, **95**, 15,365-15,394, 1990.
- Hauksson, E., State of stress from focal mechanisms before and after the 1992 Landers earthquake sequence, *Bull. Seismol. Soc. Am.*, **84**, 917-934, 1994.
- Hauksson, E., and J.S. Haase, Three-dimensional  $V_P$  and  $V_P/V_S$  velocity models of the Los Angeles Basin and central Transverse Ranges, California, *J. Geophys. Res.*, **102**, 5423-5453, 1997.
- Hauksson, E., and G.V. Saldivar, Seismicity and active compressional tectonics in the Santa Monica Bay, southern California, *J. Geophys. Res.*, **94**, 9591-9606, 1989.
- Hauksson, E., L. M. Jones, K. Hutton, and D. Eberhart-Phillips, The 1992 Landers earthquake sequence: Seismological observations, *J. Geophys. Res.*, **98**, 19,835-19,858, 1993.
- Horiuchi, S., G. Rocco, and A. Hasegawa, Discrimination of fault planes from auxiliary planes based on simultaneous determination of stress tensor and a large number of fault plane solutions, *J. Geophys. Res.*, **100**, 8327-8338, 1995.
- Jones, L. M., Focal mechanisms and the state of stress on the San Andreas fault in southern California, *J. Geophys. Res.*, **93**, 8869-8891, 1988.
- Knopoff, L., Statistical accuracy of the fault-plane problem, *Publ. Dominion Obs. Ottawa*, **24**, 317-319, 1960.
- Larson, R.J. and M.L. Marx, *An Introduction to Mathematical Statistics and Its Applications*, 536 pp., Prentice-Hall, Englewood Cliffs, N.J., 1981.
- McKenzie, D. P., The relationship between fault plane solutions for earthquakes and the directions of the principal stresses, *Bull. Seismol. Soc. Am.*, **59**, 591-601, 1969.
- Michael, A. J., Determination of stress from slip data: Faults and folds, *J. Geophys. Res.*, **89**, 11,517-11,526, 1984.
- Michael, A.J., The use of focal mechanisms to determine stress: a control study, *J. Geophys. Res.*, **92**, 357-368, 1987a.
- Michael, A.J., Stress rotation during the Coalinga aftershock sequence, *J. Geophys. Res.*, **92**, 7963-7979, 1987b.
- Michael, A.J., Spatial variations in stress within the 1987 Whittier Narrows, California, aftershock sequence: New techniques and results, *J. Geophys. Res.*, **96**, 6303-6319, 1991.
- Michael, A.J., W.L. Ellsworth, and D.H. Oppenheimer, Coseismic stress changes induced by the 1989 Loma Prieta, California earthquake, *Geophys. Res. Lett.*, **17**, 1441-1444, 1990.
- Pope, A.J., Fiducial regions for body wave focal plane solutions, *Geophys. J. R. Astron. Soc.*, **30**, 331-342, 1972.
- Reasenberg, P., and D. Oppenheimer, FPFIT, FPPLOT, and FPPAGE: FORTRAN computer programs for calculating and displaying earthquake fault-plane solutions, *U.S. Geol. Surv. Open File Rep.*, **85-739**, 1985.
- Reid, H.F., The mechanics of the earthquake, in *The California Earthquake of April 18, 1906*, Carnegie Inst. of Washington, Washington D. C., 1910.
- Rice, J.R., Fault stress states, pore pressure distributions, and the weakness of the San Andreas Fault, in *Fault Mechanics and Transport Properties of Rock: A Festschrift in Honor of W.F. Brace*, edited by B. Evans and T.-f. Wong, pp. 475-503, Academic, San Diego, Calif., 1992.
- Rivera, L., and A. Cisternas, Stress tensor and fault plane solutions for a population of earthquakes, *Bull. Seismol. Soc. Am.*, **80**, 600-614, 1990.
- Seeber, L. and J.G. Armbruster, The San Andreas fault system through the Transverse Ranges from small earthquakes, *J. Geophys. Res.*, **100**, 8285-8310, 1995.
- Tarantola, A., *Inverse Problem Theory: Methods for Data Fitting and Model Parameter Estimations*, 613 pp., Elsevier Sci., New York, 1987.
- Twiss, R.J., and J.R. Unruh, Analysis of fault slip inversions; do they constrain stress or strain rate?, *J. Geophys. Res.*, **103**, 12,205-12,222, 1998.
- Wallace, R. E., Geometry of shearing stress and relation to faulting, *J. Geol.*, **59**, 118-130, 1951.
- Wessel, P., and W.H.F. Smith, Free software helps map and display data, *Eos Trans. AGU*, **72**, 441, 445-446, 1991.
- Zhao, D., H. Kanamori, and D. Wiens, State of stress before and after the 1994 Northridge earthquake, *Geophys. Res. Lett.*, **24**, 519-522, 1997.
- Zoback, M.D., et al., New evidence on the state of stress of the San Andreas fault system, *Science*, **238**, 1105-1111, 1987.

G.A. Abers, Boston University, Department of Earth Sciences, 685 Commonwealth Ave., Boston, MA 02215, USA. (abers@bu.edu)

J.W. Gephart, INSTOC, Snee Hall, Cornell University, Ithaca, NY 14853-6801, USA. (gephart@geology.cornell.edu)

(Received May 11, 2000; revised November 28, 2000; accepted June 22, 2001.)